Lattice Boltzmann simulations of tracer diffusion in microswimmer suspensions

Nordanger, Henrik

2023

Document Version:
Publisher's PDF, also known as Version of record

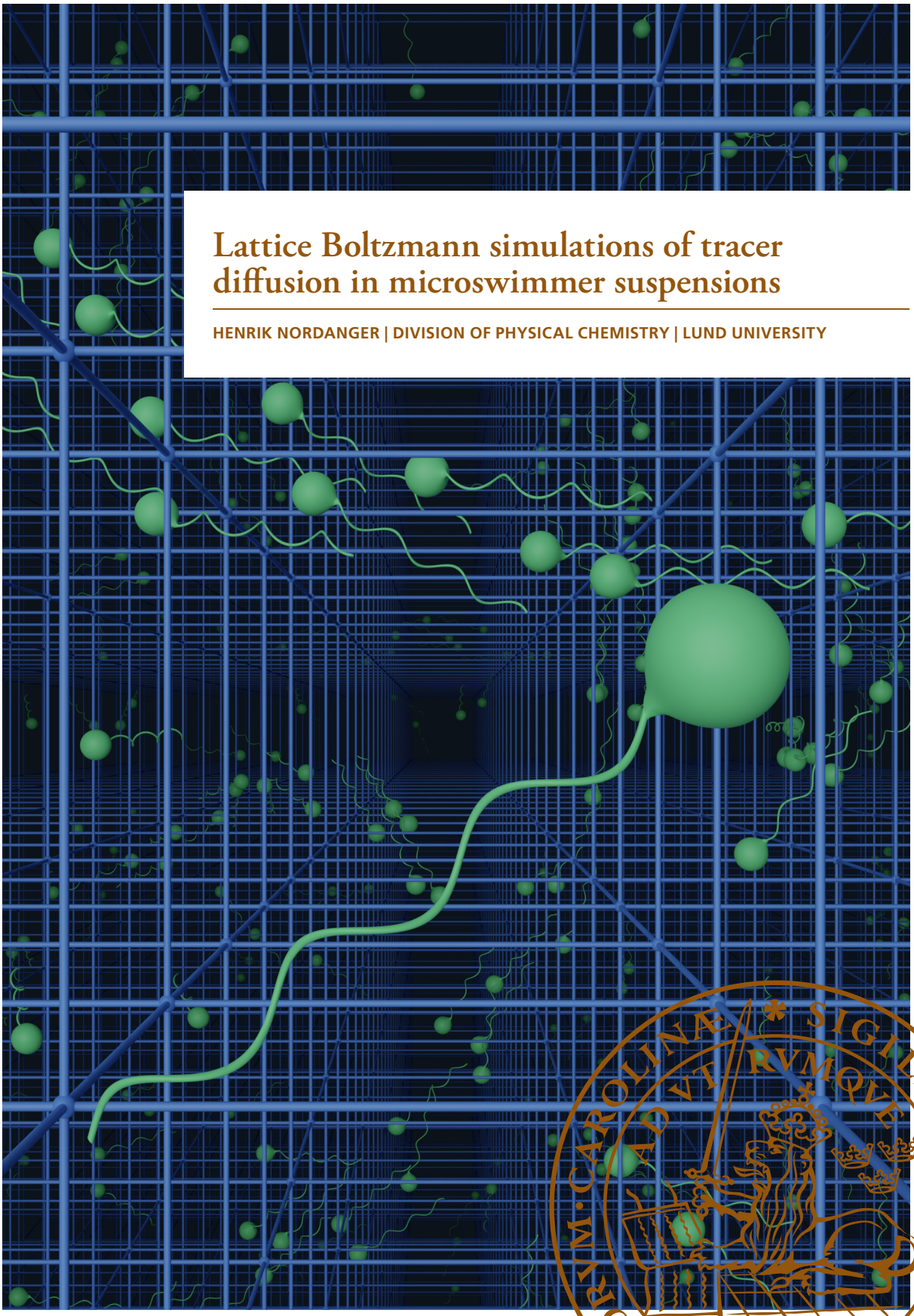

Lattice Boltzmann simulations of tracer diffusion in microswimmer suspensions

HENRIK NORDANGER | DIVISION OF PHYSICAL CHEMISTRY | LUND UNIVERSITY

Printed by Media-Tryck, Lund 2023 NORDIC SWAN ECOLABEL 3041 0903

ISBN: 978-91-7422-940-0

Physical Chemistry
Faculty of Science
Lund University

Lattice Boltzmann simulations of tracer diffusion in microswimmer suspensions

Lattice Boltzmann simulations of tracer diffusion in microswimmer suspensions

by Henrik Nordanger

LUND
UNIVERSITY

DOCTORAL DISSERTATION

by due permission of the Faculty of Science, Lund University, Sweden.
To be defended on Thursday, the 4th of May 2023 at 09:15 in Lecture hall A at the Department of Chemistry, Lund University.

Faculty opponent

Prof. Marco Polin
Mediterranean Institute for Advanced Studies (IMEDEA UIB-CSIC), Esporles, Spain

Organization
LUND UNIVERSITY
Department of Chemistry
Box 124
SE–221 00 LUND
Sweden

Document name
DOCTORAL DISSERTATION
Date of disputation
2023-05-04
Sponsoring organization
Knut and Alice Wallenberg Foundation (Project No. KAW 2014.0052).
Swedish Research Council (grant ID 2015-05449)

Author(s)
Henrik Nordanger

Title and subtitle
Lattice Boltzmann simulations of tracer diffusion in microswimmer suspensions

Abstract
Suspensions of microswimmers are a class of systems inherently out of equilibrium, due to the mechanical work continuously performed by a large number of active agents. Biological examples are plentiful, as many aquatic microorganisms have the ability to propel themselves. A distinct phenomenon displayed by such systems is the increased diffusivity of passive tracer particles, relative to their equilibrium Brownian value. Such *enhanced diffusion* is known to be of biological importance, from the microscopic level and up to geographical length scales. Active diffusion coefficients have been found to have non trivial dependence on factors such as swimmer concentration and tracer size. The complexities of the topic are especially apparent at high swimmer densities, where the hydrodynamic interactions between bacteria are known to lead to significant non-linear behavior and long-ranged chaotic flows, referred to as active turbulence, and where diffusivity is dramatically increased.

Several aspect of experimentally observed enhanced diffusion have been attributed to far-field hydrodynamic advection of tracers by dipolar microswimmers, although many remain unexplained. In this thesis, I seek to explore such phenomena using three-dimensional particle resolved Lattice Boltzmann simulations, where swimmers are modelled as extended force dipoles. Our method allows for the inclusion of large numbers of swimmers ($\geq 10^5$), as typically required for adequately reproducing collective behavior. Primarily, I focus on three diffusion-related phenomena. First, I consider the impact of Brownian motion on enhanced tracer diffusion, finding the latter to be suppressed when the Brownian diffusion coefficient is large. However, this effect appears to be negligible for biologically relevant self-propulsion speeds, a finding which is at odds with previous claims in the literature. I then investigate the tracer size dependence of enhanced diffusion, finding a non-monotonic relation qualitatively opposite to previous experimental observations. Lastly, I turn to the phenomenon of anisotropic diffusion of ellipsoidal tracers. I find tracers in pusher-type suspensions to exhibit an increase in the ratio between diffusion coefficients along their major and minor axes, coinciding with the onset of active turbulence. As experimental observations have instead shown a decrease in this ratio with swimmer concentration, we conclude that non-hydrodynamic effects have significant contributions to anisotropic diffusion.

Key words
Lattice Boltzmann, microswimmers, active matter, enhanced diffusion

Classification system and/or index terms (if any)

Supplementary bibliographical information

Language
English

ISSN and key title

ISBN
978-91-7422-940-0 (print)
978-91-7422-941-7 (pdf)

Recipient's notes

Number of pages
139

Price

Security classification

Signature _____ Date 2023-03-23

Lattice Boltzmann simulations of tracer diffusion in microswimmer suspensions

by Henrik Nordanger

LUND
UNIVERSITY

This doctoral thesis is constructed as a summary of research papers and consists of two parts. An introductory text puts the research work into context and summarises the main conclusions of the papers. Then, the research publications themselves are reproduced. The research papers may either have been already published or are manuscripts at various stages.

Cover art: *Through a lattice, darkly*, by Henrik Nordanger

Faculty of Science, Department of Chemistry, Division of Physical Chemistry

ISBN: 978-91-7422-940-0 (print)
ISBN: 978-91-7422-941-7 (pdf)

Printed in Sweden by Media-Tryck, Lund University, Lund 2023

Media-Tryck is a Nordic Swan Ecolabel certified provider of printed material. Read more about our environmental work at www.mediatryck.lu.se

MADE IN SWEDEN

Dedicated to my honored wife
Rebecka
and my wonderful children
Freja – Ronja – Viggo

Table of Contents

Acknowledgments

Like many others before me, I feel immense gratitude for my time as a PhD student, and toward all the people who have supported me in the grand quest which has now culminated in this thesis. There are so many to thank, both for all the science-related interactions I've had, but also for the friendships I've made, the interesting people I've gotten to know, and all of the plain fun I've had. In truth, that extends to every single person at the divisions of Physical Chemistry and Theoretical Chemistry, as well as to other friends and family. Unfortunately, I cannot mention you all by name. I have endeavored to address as many of you as is practically reasonable, but would all the same like to apologize in advance to anyone who might feel overlooked.

The first, and hopefully most obvious thanks should go to my main supervisor, **Joakim**. Thank you for your guidance, help, and support, and for always encouraging me to learn and accomplish more. I always knew that I could come to you with questions or concerns, and you would do your best to help. It was a rare occasion when you would not be available for a discussion at short notice. Also, I hope it goes without saying that in addition to a supervisor, I consider you a friend. Thank you for all the fun we've had over lunches, on walks, or when travelling. I regret not going to more of your concerts – an oversight I hope I can correct in the future.

I would also like to thank my other two supervisors, **Tobias** and **Peter**. While I never relied on you to the same degree as I did on Joakim, it was always a great comfort to know that you were available, should I have needed it. Also to you Tobias – it was great to retain a connection to physics, as you were also the supervisor for my master's thesis.

Another round of thanks should go to the members of my research group, both past and present. First and foremost, thank you **Dóra**. Even though I am the native of this town, it was you who made me feel at home at the division. You introduced me to many aspects of the workplace, and were a great office mate. Thank you for all the practical help, and of course for all the fun. Your thesis was also a great inspiration when writing my own. To **Jason** and **Ismail**, thank you for the enjoyable discussions – both scientific and otherwise. To **André**, **Shan** and **Yoshimi**, it was great having you on the team, and I hope I was of help during your time here.

For great collaborations, and for great times in Ediburgh as well as Lund – thank you **Alex** and **Viktor**.

Thank you to all of my fellow PhD students who helped organize the Christmas party I somehow ended up in charge of. Special thanks to **Erika**, **Kasia**, **Alexandra**, and **Samuel** for the extra efforts put in, especially towards the end.

Thank you **Vidar**, **Erik** and **Sara** for all the fun at our adventure in Amsterdam.

Thank you **Johan** for instructing me on and supporting my use of the Sinterface tensiometer, thank you **Victoria** for you guidance on teaching in the lab, and thank you **Ben** for instructing the students and colleagues who came to me for help on experimental techniques. I was out of my depth there. Thank you **Chris** for the technical assistance with the tensiometer (as well as other things) – especially the quick response I got when I had issues in the middle of hosting a lab. Thank you **Tommy Nylander** and **Emma** for more general advice on teaching.

For all the assistance on various issues, thank you **Helena**, **Maria Lövgren**, and **Maria Södergren**. Whenever I didn't know who to turn to for help, I went to one of you, because somehow you guys know almost everything. When you did not, you always seemed to know towards whom to direct me. Thank you **Ulf** and **Anna** for productive and enjoyable meetings and talks.

For various other interactions, thank you **Simon**, **Arif**, **Marija**, **Tommy Dam**, **Linda**, **Marco**, **Junhao**, **Axel**, **Jasper**, **João**, **Nikol**, **Jen**, and many others.

Now, to all the people outside of the workplace. First, to my most honored wife and the love of my life – **Rebecka**. Thank you for everything. You are a wonderful life partner, and I cherish all the adventures we've had together, the greatest of which has just started. You have become a great mother to our three(!) children. Thank you for being their primary caregiver while I've been taking care of this thesis.

To my children, **Freja**, **Ronja** and **Viggo**, you most numerous and adorable distractions – thank you. If you ever find this dusty old tome in one of your father's bookshelves, know that I love you very much. Thinking of you always puts a smile on my face, and I look forward to seeing you grow up.

To my mother and father, **Tina** and **Jan**, thank you for a lifetime of support. Thank you for raising me, and all of the various forms of inspiration you have given me over the years, that lead me to become a scientist. With this thesis, I think I finally feel like one. Also, thank you for all the help with the kids while I've been working.

Finally, to my mother-, and father-in-law, **Marika** and **Bengt**. Thank you also for all the support with the kids and everything else. Having had you around has been a blessing.

Popular scientific summary

In many parts of the world, it is a common occurrence to see flocks of birds performing intricate and seemingly well-coordinated maneuvers, as for show. Given the opportunity, one might see similarly fascinating movements among schools of fish, or herds of land animals. Moving together in such complex patterns can have great benefits, as it is often safer to move as a group than doing so alone. Such ordered movement, where a large number of individuals contribute, is called *collective motion*. Some forms of such behavior is well understood, but the details of why some patterns of motion appear remains difficult to explain.

Looking through a microscope, one can also see bacteria, alga, or other *microswimmers* performing collective motion. Some swim in a breast stroke-like manner using two tail-like structures called flagella, and are called *pullers*. Others have flagella at the back of their bodies which they rotate in order to swim, and are called *pushers*. The latter generally show the most exciting behavior. They tend reorient themselves to swim side-by-side, and stir up the surrounding fluid to the degree that they can move faster and over longer distances than they could on their own. As they swim, the movement of the fluid around them will spread any nutrients around over time, a phenomenon called *enhanced diffusion*. In this thesis, I have explored several aspect of such diffusion by using computer simulations. This approach allowed me to specify the details of the swimmer model as well as the environment, in order to mimic different experimental situations or simulate systems that cannot be realized in a laboratory. A number of non-swimming *tracer particles* were included, the motion of which I tracked over time to evaluate their diffusion.

Even in a fluid without microswimmers present, particles will move around slightly with what is called *Brownian motion.* One of the goals of my work has been to understand how such motion affects enhanced diffusion. Another has been to investigate how particles of different sizes are affected by enhanced diffusion. When undergoing Brownian motion smaller particles always tend to move the most, but this has been found to not always be the case for particles in microswimmer suspensions. Lastly, I studied how microswimmers affect elongated particles, and in particular how such particles are pushed around to different degrees in different directions. One would perhaps expect that a long and thin particle would be hardest to push ”sideways”, yet this is what has been seen to happen in some experiments.

The results of my simulations do not always match experimental observations made previously, but what that tells us is that the behavior of the microswimmers is not due to the hydrodynamic interactions that I have included, narrowing down the field of possible explanations and showing where more research is needed.

List of Publications

This thesis is based on the following publications, referred to by their Roman numerals:

I **Anisotropic diffusion of ellipsoidal tracers in microswimmer suspensions**

H. Nordanger, A. Morozov, J. Stenhammar
Physical Review Fluids, 2022, **7**, 013103

II **Interplay between Brownian and hydrodynamic tracer diffusion in suspensions of swimming microorganisms**

H. Nordanger, A. Morozov, J. Stenhammar
Submitted to Journal of Fluid Mechanics,
DOI: 10.48550/ARXIV.2302.13688

III **Size dependent hydrodynamic diffusion of spherical tracers in microswimmer suspensions**

H. Nordanger, A. Nüsslein, A. Morozov, J. Stenhammar
Manuscript

IV **Particle-resolved lattice Boltzmann simulations of 3-dimensional active turbulence**

D. Bárdfalvy, **H. Nordanger**, C. Nardini, A. Morozov, J. Stenhammar
Soft Matter, 2019, **15**, 7747

My contributions to the papers

Paper I: Anisotropic diffusion of ellipsoidal tracers in microswimmer suspensions

I performed the simulations and data analysis, and wrote the manuscript with input from the co-authors.

Paper II. Interplay between Brownian and hydrodynamic tracer diffusion in suspensions of swimming microorganisms

I performed the simulations and data analysis and participated in the writing of the manuscript.

Paper III: Size dependent hydrodynamic diffusion of spherical tracers in microswimmer suspensions

I performed the simulations and data analysis and participated in the writing of the manuscript.

Paper IV: Particle-resolved lattice Boltzmann simulations of 3-dimensional active turbulence

I did part of the data analysis and participated in the writing of the manuscript.

Notation

Latin alphabet

a	Effective swimmer body radius
$\tilde{a}$	Effective hydrodynamic radius of swimmer
$C_{\mathbf{p}}$	Autocorrelation function of tracer orientation
C_T	Autocorrelation function of tracer velocity
C_U	Autocorrelation function of the fluid velocity
c_s	Speed of sound
$\mathbf{c}$	Velocity vector
D_T	Translational diffusion coefficient
D_0	Passive (Brownian) diffusion coefficient
D_A	Active diffusion coefficient
D_R	Rotational diffusion coefficient
$D_{R,0}$	Rotational passive (Brownian) diffusion coefficient
$D_\parallel$	Diffusion coefficient, parallel to major axis
$D_\perp$	Diffusion coefficient, perpendicular to major axis
d	Dimensionality
$\mathbf{E}$	Rate of strain tensor
$\mathbf{F}$	Force
$\mathbf{f}$	Force density
f	Phase-space density function
f_i	Density function of particles moving at velocity $\mathbf{c}_i$
f^0	Equilibrium density function
h	Discretization length of finite difference scheme
$\mathbf{i}$, $\mathbf{j}$, $\mathbf{k}$	Cartesian basis vectors
$\mathbb{I}$	Unit tensor
L	Non-dimensionalized persistence length
δL	Lattice spacing
l	Swimmer length
l_p	Swimmer persistence length
m	Particle mass
N_s	Number of microswimmers
N_t	Number of tracers
n	Number density of microswimmers
n_c	Critical density
Pe	Péclet number
p	Pressure
$\mathbf{p}$	Orientation

$\mathbf{p}_s$	Swimmer orientation
$\mathbf{p}_t$	Tracer orientation
$\mathbf{Q}$	Nematic order parameter
q	Size of LB basis set
$\hat{q}$	Particle aspect ratio
R_0	Radius of spherical tracer
Re	Reynolds number
$\mathbf{r}$	Position
$\mathbf{r}_s$	Swimmer position
$\mathbf{r}_t$	Tracer position
T	Relaxation time
t	Time
t_0	Time origin
δt	Time step length
Δt	Time increment
$\mathbf{U}$	Fluid velocity
$\mathbf{u}_s$	Swimmer velocity
$\mathbf{u}_t$	Tracer velocity
$\mathbf{V}$	Vorticity tensor
v_s	Swimming speed
$\mathbf{W}$	Flow field generated by flagellum
w_i	Weights of velocity set

Greek alphabet

β	Shape parameter
δ	Dirac δ function
δ_p	Regularized δ function
ε	Regularization length
θ	Angle
κ	Dipole strength
κ_n	Non-dimensionalized dipole strength
λ	Tumbling frequency
μ	Dynamic viscosity
μ_b	Bulk viscosity
ρ	Mass density
τ_T	Translational correlation time
τ_R	Rotational correlation time
Φ	Forcing term
Ψ	Probability density function
Ω	Collision operator

Prologue

The aim of this thesis has been to study different aspects of enhanced diffusion in microswimmer suspensions, by means of large-scale Lattice Boltzmann simulations. Several experimentally observed phenomena remain largely unexplained, due in large part to the complexities associated with collective motion at higher swimmer concentrations, and in particular that of bacterial turbulence. I mainly considered the following three topics:

- **The interplay between active and passive diffusion.**

  We find that large values of the Brownian diffusion coefficient can lead to suppression of active diffusion, but argue that this effect is negligible for biologically relevant swimmer and tracer parameters, at odds with previous claims in the literature.

- **The effect of Faxén's law on the tracer size-dependence of enhanced diffusion.**

  The diffusion coefficient is found to exhibit non-monotonic behavior with respect to tracer size, qualitatively opposite to what has been experimentally observed. We thus argue that the experimental results cannot be explained by hydrodynamic interactions, as these are included in our simulations.

- **Anisotropic diffusion of ellipsoidal tracers.**

  In bulk suspensions of pushers, we observe a sudden increase in the ratio of diffusion coefficients along the tracers' major and minor axes, coinciding with the onset of active turbulence, while finding no anisotropic behavior in puller suspensions. This is in disagreement with previous experimental results in bacterial suspensions confined to thin liquid films, leading us to conclude that the experimentally observed behavior might be due to non-hydrodynamic effects, and that the geometry of the system might be of importance.

1 Introduction

Figure 1.1 Examples of macroscopic active matter, in the form of a flock of starlings (left, reproduced from ref. 1) and a school of barracudas (right, reproduced from ref. 2).

Most aqueous environments on earth are home to a wide range of microorganisms, from the surface of oceans and lakes where algae are often plentiful, to the seafloor where bacteria break down biological matter settling from above. Even the bodies of large organisms can act as ecosystems to vast numbers of microscopic forms of life. Many such microorganisms possess the ability to propel themselves, which they rely on to find nutrients, or to avoid hazards such as predators or toxins. As they swim they stir up the surrounding fluid, which displaces any particles or other organisms around them. The disturbance flow due to a collection of such swimmers leads to enhanced diffusion, which in itself can have great biological importance across many length scales – from the cellular level,[3] to potentially contributing to global circulation.[4] In this thesis, I have endeavored to build a better understanding of enhanced diffusion of tracer particles in microswimmer suspensions, through the use of large-scale Lattice Boltzmann simulations.

1.1 Active matter

The field of active matter concerns a class of systems intrinsically out of equilibrium, due to the presence of a large number of agents with the ability to extract energy from their environment, which they use to perform mechanical work.[5-7] Research on the topic combines aspects of physics, chemistry, and biology, as most examples of active matter are biological in origin, while many of the resulting phenomena are rationalised in terms of concepts from thermodynamics and statistical physics.

The work performed by individual agents is usually in the form of self-propulsion. While the details of the mechanics of motion are of interest in themselves, much of the focus of active matter lies in the large-scale collective motion that the propulsion often results in. Macroscopic collective motion can be observed in flocks of birds[8] and schools of fish,[9,10] giving rise to fascinating pattern formation as displayed in Fig. 1.1. On the microscopic scale, different forms of collective motion is displayed by a variety of organisms, and includes motility-induced clustering,[11] and bacterial (or active) turbulence.[12-16] The latter refers to the appearance of chaotic flow patterns seen in bacterial suspensions at high enough concentrations, where the fluid speed can greatly exceed the propulsion speed of individual swimmers.

Several theoretical models have been developed with the purpose of describing the phenomena observed in active matter, starting from basic physical principles. The non-equilibrium nature of such systems, and their often non-linear, chaotic behaviour, suggest that this is not an easy task. However, even relatively simple active matter models have been successful in qualitatively describing collective behaviour. One of the earliest models is the so-called Vicsek model, developed in 1995.[17] It is an intentionally minimal model which aims to describe flocking behaviour by employing one basic rule, through which each individual aligns with its neighbours within a given distance, with some uncertainty due to a noise. Despite its simplicity, it has proven to be able to accurately reproduce the collective motion of some groups of animals, like that of flocking birds, and remains a widely studied model. Another, similarly minimal model of active matter consists of so-called active Brownian particles. These are spherical, self-propelled particles with mutual, isotropic repulsive interactions. At high enough particle concentrations, the local velocities of the particles decrease due to collisions, and the system separates into dense and dilute phases. This is referred to as motility-induced phase separation, due to the dependence on the particle's degree of self-propulsion.[18] This bears similarities to behaviour observed in some microorganisms, like *Myxococcus Xanthus*.[19]

1.2 Microswimmers

The two models described above describe what is referred to as *dry* active matter, since they describe systems in contact with a solid substrate that acts as a momentum sink. In the case of bulk aqueous environments, the presence of a momentum-conserving fluid is instead of central importance to the dynamics to the system, as it leads to long-ranged hydrodynamic interactions between agents. Such systems are called *wet* active matter, and any microscopic self-propelled agents involved are aptly named *microswimmers*.

The study of microswimmers is of interest not only for fundamental research, but also for many applications primarily in biology and medicine.[20] Understanding the behavior and locomotion of pathogenic microorganisms is of relevance for preventing and fighting infectious diseases,[21,22] characterization of sperm motility is employed for evaluating and potentially treating infertility,[23,24] and swimming micro-scale robots have been suggested for highly targeted drug delivery,[25,26] and microsurgery.[27] In the design of such microrobots, inspiration can be drawn from the study of the naturally evolved swimming strategies of microorganisms.

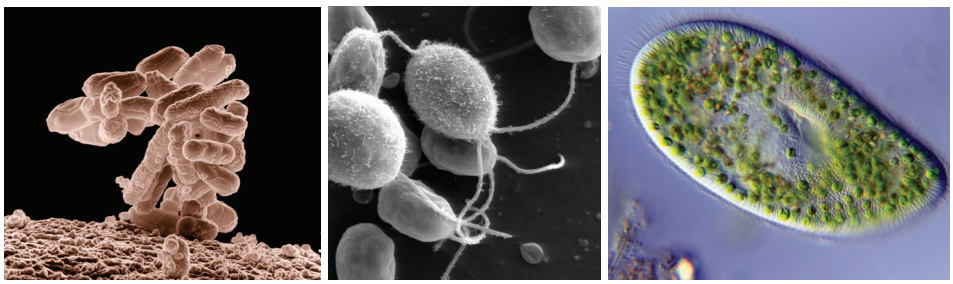

Figure 1.2 Examples of typical biological microswimmers. ***E. coli*** (left) is a flagellated pusher bacterium (reproduced from ref. 28), ***Chlamydomonas*** (middle) is a flagellated puller alga (reproduced from ref. 29), and ***Paramecium*** (right) is a ciliated alveolate (reproduced from ref. 30).

Biological microswimmers employ a wide range of mechanisms for locomotion. Some utilize one or several flagella, which can be arranged in a variety of configurations depending on the species. In general, they can be separated into two groups, depending on whether their flagella are primarily rear-, or front-mounted, relative to the direction in which they swim. Examples of so-called *pushers* include the spermatozoa of animals, which have a single flexible flagellum which they move in a whip-like fashion to propel themselves. As they swim, they draw in fluid from their sides, and push it in the forward and backward directions. *Pullers* do the opposite, by pulling fluid from their fronts and rears, and expel it towards their sides. Most swimming bacteria, as well as many other microorganisms, can be considered pushers. The bacterium *Caulobacter* has a single rigid flagellum of a right-handed helical shape attached to a rotary motor, which is turned clockwise to push the cell forwards.[31] *Escherichia coli* (Fig. 1.2 left), often considered an archetypal pusher, has several side- and rear-mounted helical flagella that bundle together when turned clockwise, and rotate as a cluster to propel the swimmer.[32] By rotating the individual flagella counter-clockwise, they unbundle and cause the bacterium to change direction. Alternation between swimming and reorientation is referred to as *run-and-tumble* behaviour, and is observed in a number of species. The alga *Chlamydomonas* (Fig. 1.2 center) is often considered a model puller-type swimmer. It has two front-mounted flagella, which it beats in a synchronized, breast stroke-like manner to move itself.[33] It has however been noted that it oscillates between effectively being a pusher and puller during a stroke cycle,[34,35] and pure

puller-like behaviour is rarely seen in biological microswimmers. Many forms of collective behaviour in wet active matter, most notably that of bacterial turbulence, can be partially of fully attributed to to the hydrodynamic interactions between pushers, making them especially interesting subjects of study.[36]

Some microorganisms, in particular eukaryotic ones, move by using a large number of cilia covering their entire cell bodies. These beat in an organized, wave-like pattern to propel the swimmer, in what is called a metachronal rhythm.[37] *Paramecium* (Fig. 1.2 right) is an organism representative of this group, whose members cannot always be classified as either pushers or pullers. Unlike flagellated microswimmers, the actuation of a ciliated organism is generally not limited to the rear or front of its body, and propulsive forces are instead generated across most of its surface area.

1.3 Biomixing and enhanced diffusion

It is well known that the presence of swimming organisms in an aqueous environment leads to increased mixing of the fluid constituents.[38] As an organism swims, it disturbs the fluid around it, thereby displacing any particles in its vicinity. This advection increases in magnitude with increased density of swimmers in the system, and can often come to dominate over displacements due to passive diffusion. This can be seen in Fig. 1.3, which displays trajectories of spherical tracer particles in suspensions with and without swimming bacteria.

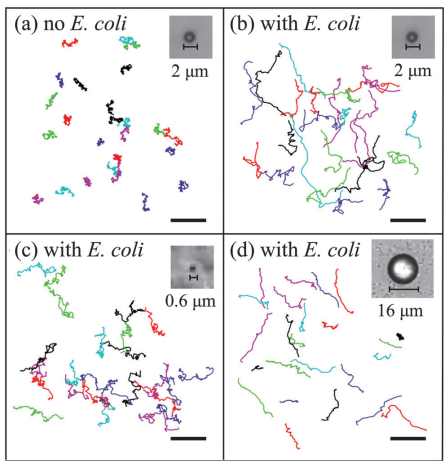

Figure 1.3 Experimentally measured trajectories of spherical particles in suspensions without microswimmers (a), and in the presence of ***E. coli*** (b-d). The bacterial concentration was $n = 3 \times 10^9$ cells per ml, the observation time was 8 s, and the scale bars are 20 μm. It can be readily seen that the presence of bacteria enhances particle displacements. Tracer sizes are indicated in the top right of each panel. Reproduced from ref. 39 with permission.

Quantitatively, the impact of particle advection by microswimmers can be seen in the increase in effective translational diffusion coefficients D_T in active suspensions, relative to that of Brownian motion. This phenomenon is referred to as *enhanced diffusion*,[40-43] and will be discussed more extensively in Chapter 5. In dilute suspensions, D_T is known to increase linearly with microswimmer concentration n,[38,41,43] but displays non-trivial behavior following the onset of collective behaviour. In suspensions of pushers, the scaling becomes superlinear, while progressing slower than linearly for pullers.[44-47] At a critical density of pushers, corresponding to the onset of bacterial turbulence, the effective diffusion coefficient is known to increase dramatically.[44]

This is closely related to active transport, and is of importance in many biological contexts. For example, the collective behaviour in colonies of flagellated protozoa is known to increase their fluid supply, and thereby their access to nutrients.[3] It has also been hypothesized that swimming organisms contribute significantly to mass transport in the oceans, potentially supplementing global circulation and thereby affecting climate.[4,48,49] More modest, but well established instances of active transport are those occurring in intracellular transport[50] and during the absorption of nutrients in intestines,[51] although these are related to biological processes other than swimming. Advection of passive particles is also of a more fundamental relevance, as tracers can be used as probes for exploring active matter systems – especially the strongly non-equilibrium fluctuations that arise in active systems and that are fundamentally different to the corresponding fluctuations seen in equilibrium (Brownian) systems.[52]

2 Fluid dynamics

2.1 Navier–Stokes equations

In fluid dynamics, the Navier-Stokes equations are of central importance. They are partial differential equations that describe the flow of Newtonian fluids, by relating the velocity $\mathbf{U}(\mathbf{r}, t)$ of a fluid with density ρ, and dynamic and bulk viscosities μ and μ_b respectively, to the pressure p and external force density $\mathbf{f}$ acting on the fluid:[53]

$$\rho\left\{\frac{\partial U}{\partial t} + (\mathbf{U}\cdot\nabla)\mathbf{U}\right\} = -\nabla p + \mu\nabla^2\mathbf{U} + \left(\mu_b + \frac{1}{3}\mu\right)\nabla\left(\nabla\cdot\mathbf{U}\right) + \mathbf{f} \tag{2.1}$$

$$\frac{\partial\rho}{\partial t} + \nabla\cdot(\rho\mathbf{U}) = 0 \tag{2.2}$$

Equation (2.1) is referred to as the momentum equation, and Eq. (2.2) as the continuity equation. For many applications, including the simulations described in this thesis, the fluid can be considered to be incompressible - an approximation which yields the *incompressible Navier-Stokes equations*:[5,53-55]

$$\rho\left\{\frac{\partial\mathbf{U}}{\partial t} + (\mathbf{U}\cdot\nabla)\mathbf{U}\right\} = -\nabla p + \mu\nabla^2\mathbf{U} + \mathbf{f} \qquad \nabla\cdot\mathbf{U} = 0 \tag{2.3}$$

Both versions of the equations are non-linear, making most problems involving them difficult or impossible to solve analytically. Instead, elaborate numerical methods have to be employed, which is the primary concern of the branch of computational fluid dynamics.

The left-hand side of the momentum equations correspond to inertial effects, while the terms on the right-hand side describes the effects of viscous and external forces. The ratio of those two contributions is referred to as the *Reynolds number*:

$$\mathrm{Re} = \frac{\text{Inertial forces}}{\text{Viscous forces}} = \frac{\rho U l}{\mu}, \tag{2.4}$$

where U and l are the characteristic flow speed and length scale of the system in question. At low Reynolds numbers flows are laminar, meaning characterized by the fluid moving along smooth paths in layers with little to no mixing. In contrast, at high enough Reynolds numbers flows become turbulent, undergoing chaotic changes in pressure and direction over time. A characteristic of such a system is the appearance of vortices across a range of length scales. The transition from laminar to turbulent

flow occurs around a critical value of the Reynolds number, Re_{cr}, which depends on what system is being considered. For flow in a circular duct, $\mathrm{Re}_{cr} \approx 2100$,[56] while in the case of flow around an object immersed in fluid, Re_{cr} in the range of 10-100 has been observed.[53] At very low Reynolds numbers, $\mathrm{Re} \ll 1$, one can observe so-called *Stokes flow* – a special case of laminar flow where inertial effects are negligible. Illustrations of laminar and turbulent flows can be seen in Fig. 2.1.

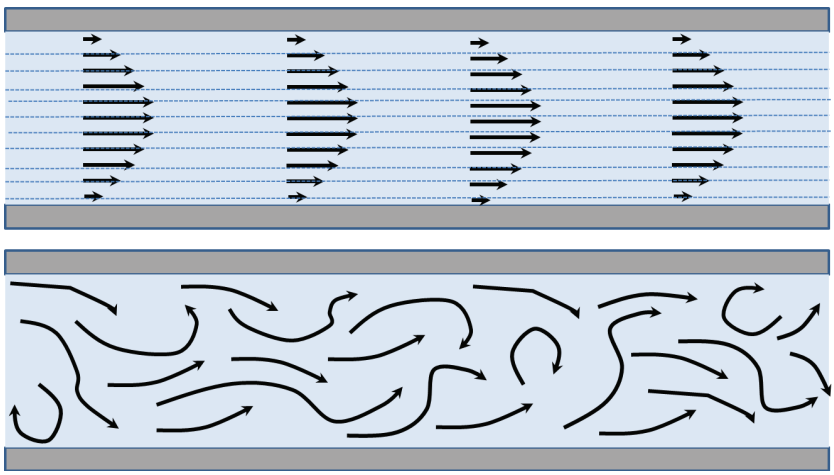

Figure 2.1 Two cases of fluid flow through a pipe. At low Reynolds numbers (top) the flow is laminar, and follows smooth streamlines that remain stable over time. At high Reynolds numbers (bottom) the flow is turbulent, with rapidly shifting streamlines. Reproduced from ref. 57.

To understand the swimming strategies of different organisms, it is useful to consider the Reynolds number of their environments. A typical bacterium has a size on the order of 1 µm, and a swimming speed on the order of 10 µm/s. In water, which has a density of around 1000 $\mathrm{kg/m^3}$ and a dynamic viscosity of around 10^{-3} $\mathrm{Pa \cdot s}$, we obtain $\mathrm{Re} \approx 10^{-5}$. If we instead consider a human being, using $l = 1$ m and $U = 1$ m/s, we obtain $\mathrm{Re} = 10^6$. In the former case, viscous forces thus dominate over inertial forces, while for the swimming human the opposite is true. The implications of this are important for what swimming mechanisms are effective at the microscale versus the macroscale.

2.2 The low Reynolds number regime

As the focus of this thesis lies on microswimmers, we now further consider the limit of low Reynolds numbers. As inertial forces are negligible in such systems, organisms such as bacteria and algae have to employ swimming gaits that do not utilize inertia, as macroscopic animals do. One aspect of this can be illustrated through the *scallop*

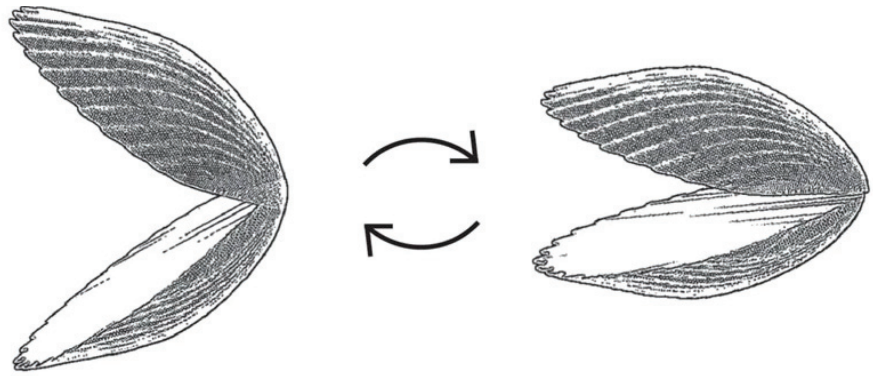

Figure 2.2 The main swimming stroke of a scallop. This animal swims, or "jumps", by repeatedly opening and closing its valves. The opening is done slowly, resulting in little displacement, while the closing is much more rapid, causing brief but significant motion. Reproduced from ref. 60.

theorem. It states that, in a Newtonian fluid at low Reynolds number, any swimmer that exhibits only time-symmetric motion will achieve no net displacement.[58] In other words, if the swimmer in question deforms its body in a sequence which is identical when observed forward and backwards in time, called *reciprocal motion*, it will always remain in the same spot after reverting to its original shape. This is true even in the case of different parts of the motion being performed at different rates. The eponym of the theorem, the scallop, is an example of a macroscopic organism swimming using such motion. It "jumps" by repeatedly opening its valves slowly and then rapidly closing them, thereby pushing water away to propel itself, as illustrated in Fig. 2.2. This mechanism is entirely dependent on inertia, and microscopic swimmers can thus not utilize it in a Newtonian fluid. The scallop theorem does however not hold in fluids not belonging to this category.[59] This has been demonstrated e.g. by the designing of a microscopic scallop-like swimmer being able to propel itself in a shear thickening fluid.[60] Biological microswimmers have developed a range of swimming mechanisms to avoid reciprocal motion. Spermatozoa and many single-celled eukaryotes have flexible flagella, which they move in a whip-like manner, sending traveling waves backwards and thereby display time asymmetry.[61] Bacteria with rigid flagella such as *Caulobacter* and *E. Coli* turn these continuously in one direction for uninterrupted locomotion.[5,62] Some swimmers have the ability to change the direction of flagellar rotation, and thereby have a simple mechanism for moving in reverse.[31] Other organisms, like *Chlamydomonas Reinhardtii*, have several flagella which they move in more complex, non-reciprocal manners.

2.3 The Stokes equations and flow singularities

Constraining ourselves to the zero Reynolds number limit relevant to microswimmers, we can neglect the inertial terms on the left-hand side of the incompressible Navier-Stokes equations, Eq. (2.3). This yields the *Stokes equations*:[55]

$$\nabla p = \mu \nabla^2 \mathbf{U} + \mathbf{f} \qquad \nabla \cdot \mathbf{U} = 0 \tag{2.5}$$

In contrast to the full Navier-Stokes equations, these are *linear* partial differential equations, and therefore significantly easier to solve. That is not to say that they are always analytically solvable, however closed-form solutions exist for a number of systems - including some relevant to the treatment of microswimmers.

We now consider a particular method of solving the Stokes equations, namely through the use of so-called Green's functions. To start, one lets the forcing term in the Stokes equations be represented by a point force $\mathbf{F}'$ at the origin, $\mathbf{f}(\mathbf{r}) = \delta(\mathbf{r}) \cdot \mathbf{F}'$, where δ is the Dirac delta function. Assuming that $|\mathbf{U}|$ and p vanish as $|\mathbf{r}| \to \infty$, the following solution can be obtained:[63,64]

$$\mathbf{U} = \mathbf{F}' \cdot \mathbb{J}(\mathbf{r}) = \frac{\mathbf{F}'}{8\pi\mu} \left(\frac{\mathbb{I}}{r} + \frac{\mathbf{r}\mathbf{r}}{r^3} \right), \tag{2.6}$$

where $r = |\mathbf{r}|$, $\mathbb{I}$ is the identity matrix, and $\mathbb{J}$ is the Green's function for the Stokes equation. In general, a Green's function is the solution G to a differential equation $\mathcal{L}G = \delta$, where $\mathcal{L}$ is a linear differential operator. The particular Green's function $\mathbb{J}$ in Eq. (2.6) is called the *Stokeslet*,[64] as it is the solution to a delta forcing in the Stokes limit. Furthermore, due to the linearity of the Stokes equations, it is straightforward to expand to more complex force distributions by a superposition of solutions. In fact, a solution to any arbitrary force distribution $\mathbf{f}(\mathbf{r})$ can be written as

$$\mathbf{U}(\mathbf{r}) = \int \mathbf{f}(\mathbf{r}') \cdot \mathbb{J}(\mathbf{r} - \mathbf{r}') \, \mathrm{d}\mathbf{r}'. \tag{2.7}$$

If the force distribution is non-trivial, the integral might not be possible to solve exactly. In such cases, it can instead be Taylor expanded. This yields a multipole expansion, of which the leading term is the Stokeslet, Eq. (2.6), representing a force monopole. The second term in the expansion represents a force dipole, and is given by[5]

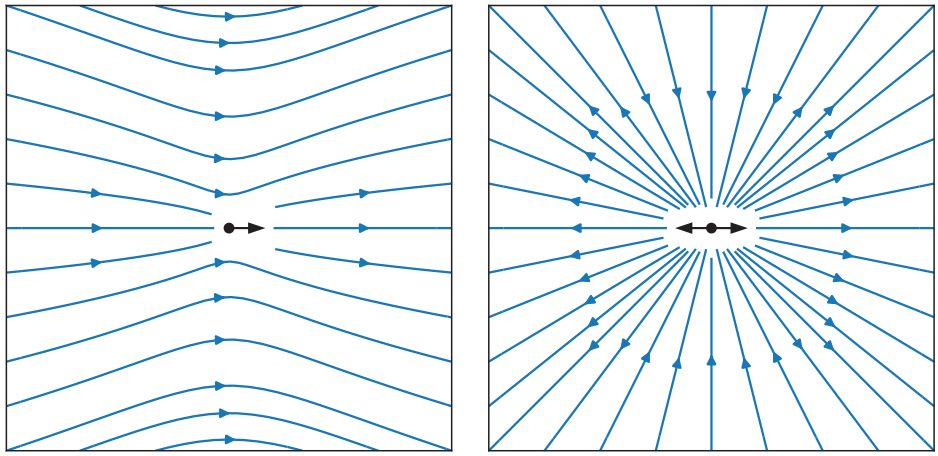

Figure 2.3 Stokes flow due to a force monopole (left) and dipole (right), referred to as a Stokeslet and stresslet respectively.

$$\mathbf{U} = \frac{\kappa}{8\pi}\left[\frac{3\left(\mathbf{p}\cdot\mathbf{r}\right)^2}{r^5} - \frac{1}{r^3}\right]\mathbf{r}, \tag{2.8}$$

where $\mathbf{p}$ is the orientation vector of the force dipole, and κ is the dipole strength, which for an extended dipole of two opposite forces $\pm F$ separated by a distance l, is given by

$$\kappa = \frac{Fl}{\mu}. \tag{2.9}$$

Just as Eq. (2.6) is associated with a Stokeslet, the form of Eq. (2.8), representing a force dipole, is associated to a so-called *stresslet*. As the force F can take on either positive or negative sign, corresponding to the two forces pointing away from or towards each other respectively, the sign of κ indicates which of the two types of dipole is being considered.

The flow fields due to a Stokeslet and a stresslet can be seen in Fig. 2.3, where the former decays as $1/r$, and the latter as $1/r^2$. The Stokeslet is the leading-order term describing the flow field around bodies with external forcing, such as a colloid being dragged through a fluid or sedimenting under gravity. The less long-ranged stresslet is, as we will see in Chapters 3 and 4, the leading-order flow singularity for force-free microswimmers.

3 Interactions in microswimmer suspensions

3.1 The flow fields of pushers and pullers

The interactions between a microswimmer and the surrounding fluid, and by extension the interactions with other particles, depend on the details of how it propels itself. As mentioned in Section 1.2, microswimmers can generally be classified as either *pushers* or *pullers*. The former class can be described as rear-actuated, where the swimmers expel fluid from their fore and aft as they move, while drawing in fluid from their sides. Pullers affect their surroundings in the opposite way, by attracting fluid along their main axis and expelling it perpendicularly to it. Fig. 3.1 schematically illustrates the flow fields that can be observed around an *E. coli* bacterium – a typical pusher, and a *C. reinhardtii* alga during the puller phase of its stroke.

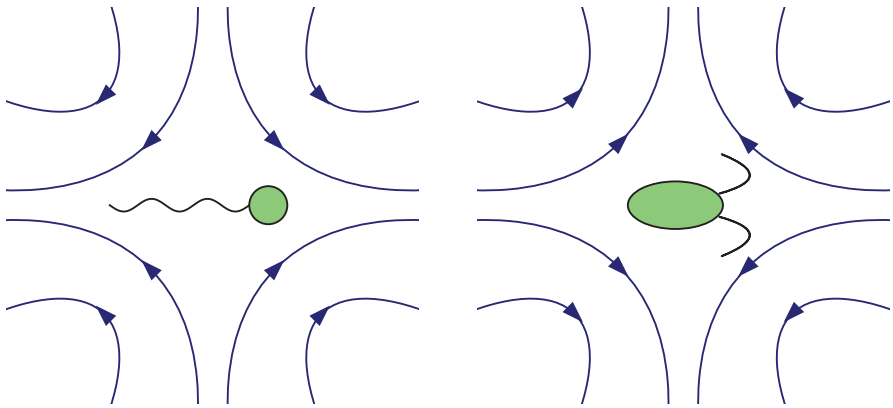

Figure 3.1 Fluid flow fields around a typical pusher like ***E. coli*** (left) and a typical puller like ***C. reinhardtii*** (right).

It can be noted that the flow field due to a pusher-type swimmer displays qualitative similarities with that of a stresslet of positive dipole strength, shown in Fig. 2.3. It turns out that the experimentally measured flow field around pusher bacteria can indeed be accurately described as that coming from an extended force dipole. This is illustrated in Fig. 3.2, which displays the flow field around an *E. coli* bacterium (A), the best fit to an extended dipole field (B), as well as the residual flow field (C), obtained by subtracting the latter from the measured flow.[65] For distances from the cell body exceeding $\sim$ 6 µm, the flow generated by the bacterium is well-approximated by that of an extended force dipole,[65] indicating that such a model would be suitable for describing the far-field hydrodynamic interactions acting in real bacterial suspensions. The implementation of en extended force dipole model is further described in Section 4.2. It is however clear, that this approach is not sufficient for capturing near-field hydrodynamic interactions. While the flow field around a swimmer has been found to be dipolar to leading order, higher-order terms in the multipole ex-

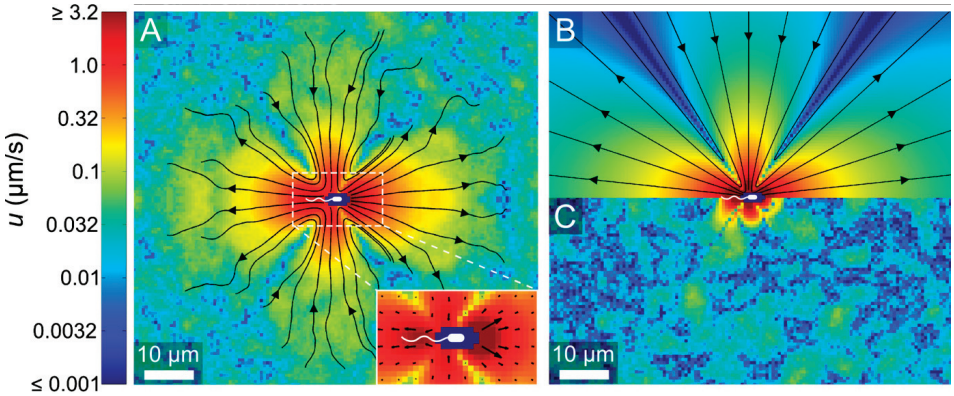

Figure 3.2 Experimentally measured flow field of an E. coli bacterium (A), the best fit dipole field (B), and the difference between the two (C), obtained by subtracting (B) from (A). The dipole model overestimates the field close to the bacterium, particularly at distances $\lesssim 6\mu\mathrm{m}$. Reproduced from ref. 65.

pansion discussed in Section 2.3 (in particular the quadrupole moment) contribute significantly close to the swimmer.[66] In addition, non-hydrodynamic effects such as excluded volume and steric interactions play important roles in real microswimmer suspensions, and their inclusion is therefore relevant for a complete description of how swimmers interact. At low to moderate microswimmer concentrations, the long ranged $(1/r^2)$ nature of dipole interactions makes them dominate over other, more short-ranged forms of interaction. In the research contained in this thesis, and for studying the generic properties of microswimmer suspensions, we will therefore limit ourselves to consider purely dipolar interactions.

3.2 Swimmer-swimmer interactions

As a microswimmer displaces the fluid around it, other particles in its vicinity will be advected and rotated. Hydrodynamic interactions between two swimmers will thus affect both of their velocities and orientations, the details of which are highly dependent on whether they can be classified as pushers or pullers. This can be exemplified by considering two swimmers moving in parallel directions, at relative positions $\mathbf{r} = \mathbf{r}_2 - \mathbf{r}_1$. If travelling precisely side by side, $\mathbf{p} \cdot \mathbf{r} = 0$, and Eq. (2.8) becomes remarkably simple:

$$\mathbf{U} = -\frac{\kappa}{8\pi r^3}\mathbf{r} \tag{3.1}$$

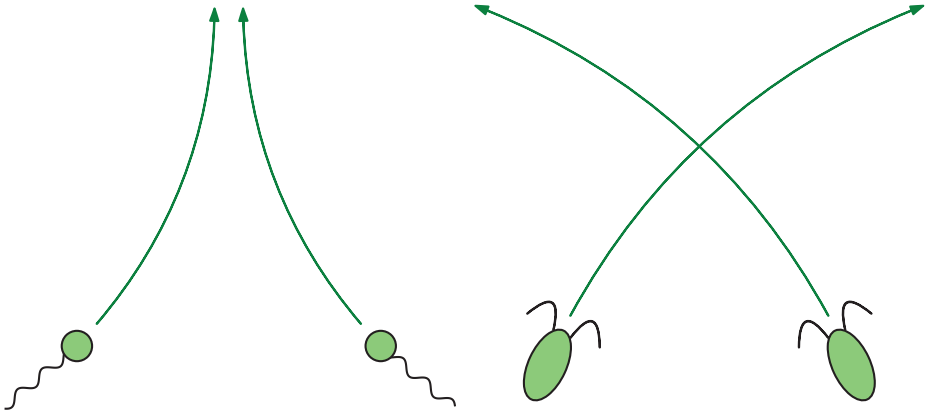

Figure 3.3 Mutual reorientation between pushers (left) and pullers (right), due to dipolar hydrodynamic interactions. Pushers align and proceed to swim side by side, while pullers turn to swim at an 180° angle.

From this it can immediately be observed that two parallel pushers ($\kappa > 0$) attract one another, while two pullers ($\kappa < 0$) in the same configuration are mutually repelled.[5,67] In addition to this, a more important effect is the mutual reorientation of the swimmers that occur due to the gradient of their flow fields, illustrated in Fig. 3.3. When two pushers come in close proximity, their swimming directions tend to align, whereby they come to swim side-by-side as their trajectories converge. Two pullers, on the other hand, tend to anti-align at an 180°angle, leading to them swimming apart.[5,67] Thus, far-field hydrodynamic interactions mediated by force dipole flow fields promote mutual alignment in the case of pusher-type microswimmer suspensions, while having an opposite, destabilizing effect on alignment in puller suspensions. The organizing effect due to hydrodynamic interactions between pusher bacteria like *E. coli* is however counterbalanced by the randomizing effect of bacterial tumbling (see Section 1.2), which plays a similar role as temperature in equilibrium systems of interacting particles.

Another aspect of microswimmer behavior of biological importance is that which occurs near a boundary. Due to differences in the hydrodynamic interactions with their environment, the dynamics greatly depend on the propulsion mechanism, just as in the case of mutual reorientation discussed above. Pusher-type swimmers tend to align themselves with solid walls, similar to how they would relative to another pusher.[5,68,69] For a swimmer such as *E. coli*, the oppositely exerted torques from its cell body and flagella then causes it to swim in a circular pattern parallel to the wall.[69-74] Pullers, on the other hand, reorient themselves as to swim at a right angle relative to the boundary, and therefore tend to swim head-on into the wall, where they therefore accumulate.[5]

3.3 Collective behavior in active matter

The interactions between microswimmers in a suspension affects both their spatial and orientational correlations, which increasingly impacts the dynamical properties of the system as the swimmer concentration n increases.[44] When reaching a critical value n_c, the correlations between pushers give rise to collective motion called *active* or *bacterial turbulence*. The turbulent state is characterized by large-scale coherent motion, where the fluid speeds can significantly exceed the propulsion speed of an individual swimmer, and is thus a strongly many-body phenomenon. In bulk suspensions of pullers, collective phenomena such as active turbulence are absent. As the dipole field around such swimmers act to decorrelate their orientations, collective motion is suppressed rather than enhanced once swimmer-swimmer correlations become significant. The transition to active turbulence has traditionally been described via mean-field kinetic theories that neglect swimmer-swimmer correlations below n_c. However, it was recently shown that such correlations have a clear impact on the properties of the suspension even far below the transition to bacterial turbulence, at concentrations corresponding to $< 10\%$ of n_c.[44] Due to the strongly non-linear behaviors in the turbulent state, a theoretical description of active turbulence is challenging. Several successful approaches have been developed, which aim to capture the complexities of this topic. Here, we briefly describe two such theoretical approaches: kinetic theory, which is a method suitable for describing bacterial turbulence among microswimmers, and active nematics, which is a model that can be utilized for capturing active turbulence in dense active matter systems.

3.3.1 Kinetic theory of microswimmer suspensions

One approach to theoretically describing active matter systems is that of *kinetic theory*. The starting point of such methods is the equations of motion (EOMs) of the particles involved.[45,75,76] Microswimmers are typically modelled as force dipoles acting on the surrounding fluid, with the sign of their dipole differing depending on if they are pushers or pullers. The system is then described by a continuum probability density function for N_s swimmers $\Psi(\mathbf{r}_1, \mathbf{p}_1, ..., \mathbf{r}_{N_s}, \mathbf{p}_{N_s}, t)$, the time evolution of which is given by the Fokker-Planck equation:[45,77,78]

$$\frac{\partial \Psi}{\partial t} + \sum_{i=1}^{N_s} \left[\nabla_{\mathbf{r},i} \cdot (\dot{\mathbf{r}}_i \Psi) + \nabla_{\mathbf{p},i} \cdot (\dot{\mathbf{p}}_i \Psi) \right] = -N_s \lambda \Psi + \frac{\lambda}{4\pi} \sum_{i=1}^{N_s} \int d\mathbf{p}_i \Psi, \quad (3.2)$$

where λ is the tumble rate of the swimmers, and the dot ($\dot{}$) represents the temporal

derivative. The flux $\dot{\mathbf{r}}$ is connected to the equation of translational motion, which has contributions due to swimming, advection from the local flow field, and translational diffusion:[75,79]

$$\dot{\mathbf{r}} = v_s\mathbf{p} + \mathbf{U}(\mathbf{r}) - D_0\nabla_{\mathbf{r}}(\ln\Psi), \tag{3.3}$$

where v_s is the swimming speed, and D_0 is the Brownian diffusion coefficient. $\dot{\mathbf{p}}$ is given by *Jeffery's equation*, which originally describes the reorientation of an ellipsoidal body in a viscous fluid at low Reynolds number,[80] plus an additional term representing rotational diffusion:[75,79]

$$\dot{\mathbf{p}} = (\mathbb{I} - \mathbf{pp}) \cdot \left[(\beta\mathbf{E} + \mathbf{V}) \cdot \mathbf{p} - D_{R,0}\nabla_{\mathbf{p}}(\ln\Psi)\right] \tag{3.4}$$

where $\mathbb{I}$ is he identity matrix, β is a shape parameter, $\mathbf{E}$ and $\mathbf{V}$ are the fluid rate of strain and vorticity tensors respectively, and $D_{R,0}$ is the rotational Brownian diffusion coefficient. A shape parameter of $\beta = 0$ corresponds to spherical swimmers, while $\beta = 1$ corresponds to infinitely thin, needle-like swimmers. We will discuss equations of motion in greater detail in Chapter 4.

Starting from a homogeneous and isotropic base state in a bulk 3-dimensional system, linear stability analysis of the mean-field version of the Fokker-Planck equation (3.2) can be performed within the framework of kinetic theory. The results show an oriental instability in the case of pushers exceeding a critical density $n_c = 5\lambda/\beta\kappa$,[44,75,76,81] which can be interpreted as a transition to active turbulence.[45,82] Puller suspensions do however prove to be stable at all swimmer densities, analogous to such systems not exhibiting significant collective phenomena. Furthermore, numerical simulations of the mean-field version of Eq. (3.2) yield flow patterns and particle motion in qualitative agreement with experimental observations, including chaotic, large-scale coherent motion.

3.3.2 Active nematics

The second main class of models exhibiting active turbulence is *active nematics*, which build on classical continuum models developed for liquid crystals.[83] This analogy stems from the fact that some active matter systems, like dense suspensions of elongated bacteria or filamentous particles mixed with motor proteins, share many characteristics with nematic liquid crystals, including long-range orientational order. The base of this approach are a set of continuum equations, describing equilibrium nematic liquid crystals:[83]

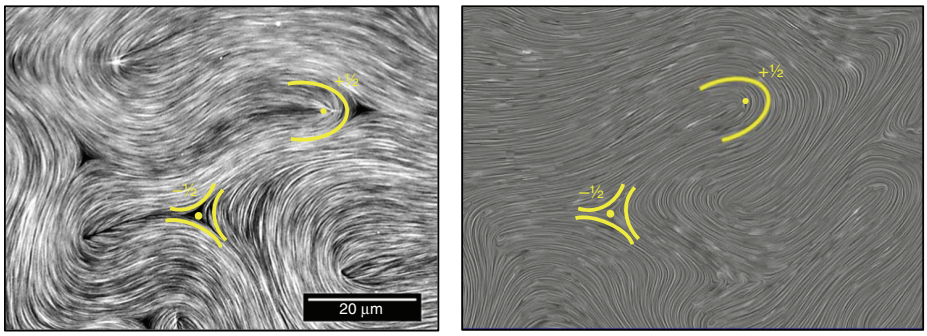

Figure 3.4 Active nematic turbulence, as observed in a microtubule-kinesin system using fluorescence confocal microscopy (left), and in simulations solving the continuum equations of motion of active nematics (right). Two defects, respectively referred to as comet-like (or +1/2), and trefoil-like (or −1/2), are highlighted in each case. Reproduced from ref. 83.

$$\frac{\partial \mathbf{Q}}{\partial t} + \mathbf{U} \cdot \nabla \mathbf{Q} - \mathbf{S} = D_R \mathbf{H}. \tag{3.5}$$

$\mathbf{Q}$ is the nematic order parameter given by $\mathbf{Q} = \frac{d}{d-1} Q(\mathbf{pp} - \mathbb{I}/d)$, where d is the dimensionality of the system, and Q is the magnitude of the local nematic order. $\mathbf{S}$ is a co-rotation term;

$$\mathbf{S} = (\beta \mathbf{E} + \mathbf{V}) \cdot \left(\mathbf{Q} + \frac{\mathbb{I}}{3} \right) + \left(\mathbf{Q} + \frac{\mathbb{I}}{3} \right) \cdot (\beta \mathbf{E} - \mathbf{V}) - 2\beta \left(\mathbf{Q} + \frac{\mathbb{I}}{3} \right) (\mathbf{Q} : \nabla \mathbf{U}), \tag{3.6}$$

and $\mathbf{H}$ relates to the relaxation of $\mathbf{Q}$ towards the the local free energy minimum;

$$\mathbf{H} = -\frac{\delta A}{\delta \mathbf{Q}} + \frac{\mathbb{I}}{3} \mathrm{Tr} \left(\frac{\delta A}{\delta \mathbf{Q}} \right), \tag{3.7}$$

Where A is the free energy density, typically taken to be of a generic, double-well form.

The flow of the surrounding fluid is described by coupling these equations to the incompressible Navier-Stokes equation, Eq. (2.3), and adding an active stress term $-\nabla \cdot (\zeta \mathbf{Q})$ to the right-hand side due to the activity of the particles. The sign of the activity coefficient ζ indicates if the system is pusher-, or puller-like in behavior, in this context often referred to as extensile or contractile. Microtubule and kinesin suspensions are an example of an extensile system suitable for modeling using active nematics,[83] while mouse fibroblast cells are a suitable candidate for a corresponding contractile system.[84]

The most significant difference between active nematics and the liquid crystal models on which they are based lies in the topological defects that form (and disappear) in pairs due to the activity.[83] An example of this can be seen in Fig. 3.4, where pairs of defects are highlighted. As these defects are generated, they can move away from one another, and pairs potentially become unbound before meeting other defects, whereby they annihilate.[85] Defects such as these appear also in equilibrium (passive) liquid crystals, but proliferate to a much higher degree in extensile active matter systems, where they are mutually repelled and therefore more long lived.[85,86] Additionally, spontaneous unbinding of defect pairs has not been observed in equilibrium nematic crystals.[85] The disruption of long-range order induced by defect proliferation, and the accompanying formation of seemingly chaotic patterns, are characteristic properties of active turbulence,[83] just as in the case of pusher microswimmer suspensions (see Fig. 3.4). Due to the continuum nature of these models, they are however limited when it comes to mapping the field-theoretical parameters to properties of individual agents. Therefore they are less suitable for modelling interactions at the length scale of an individual particle. Also, as nematic alignment is an inherent aspect of active nematics, orientational order is typically present even in the absence of activity. In the case of bacterial suspensions, this is however only true in cases of high density and/or confinement, where excluded-volume constraints (rather than activity) can cause nematic order. Thus, active nematic models are more suited for the description of experimental systems where the density is high enough to cause strong local alignment between agents, such as in Fig. 3.4.

4 Models and Methods

4.1 Overview

In this thesis I present simulations of microswimmer suspensions, with the primary purpose of studying the motion of passive tracer particles. The flow of the fluid itself is computationally solved for using the *Lattice Boltzmann method* (LBM). This is a class of methods in computational fluid dynamics which differs from others in the field, as it does not directly solve any conservation equations (namely the Navier-Stokes equations), which preserve macroscopic quantities like mass, momentum and energy. Instead, Lattice Boltzmann methods models the fluid on a mesoscopic scale as consisting of fictive particles undergoing collision and streaming processes. The particles are confined to a lattice, on which fluid properties like density and velocity can be extracted. As the dynamics of the model are local in nature, LBMs have several advantages over other approaches in computational fluid dynamics. It can be used for simulating multi-phase flows, flows through complex boundaries, and is straightforward to parallelize. For our purposes, of great relevance is the ability to incorporate a large number of off-lattice swimmers ($N_s \geq 10^5$) in order to adequately capture collective phenomena.

To model the individual microswimmers, the extended force dipole model was used, as introduced in Section 3.1. We define the equations of motion (EOMs), Eqs. (4.1) to (4.3), which determine how swimmers are advected and rotated by the fluid as well as how they propel themselves. In turn, the forces exerted by the swimmers onto the fluid determine how the flow field $\mathbf{U}$ evolves in time. While the fluid is simulated on the lattice, the swimmer (and tracer) particles have no such restrictions, and move freely in continuous space. This means that interpolations are required from the on-lattice fluid, to advect and rotate the off-lattice swimmers, and in the reverse direction, in order to apply the swimmer forces onto the fluid. Tracers are advected (and in some cases rotated) by the fluid similarly to swimmers, but exert no forces on it.

4.2 Swimmer model

In this section, we first consider the simple extended force dipole model used in the work described in this thesis, followed by a brief overview of other swimmer models of relevance in the field.

4.2.1 The extended force dipole model

In our simulations, microswimmers are modelled as consisting of a sphere of radius a connected by a thin rod to a point some distance l away. The sphere corresponds to the cell body, and the external point represents the flagellar bundle. $\mathbf{p}_s$ is a vector pointing along the rod toward the head of the swimmer, defining its orientation. Two oppositely directed forces $\pm F\mathbf{p}_s$ are exerted on the surrounding fluid, situated at the cell body and flagella respectively, thus forming an extended force dipole. l is used as a basic measure of the swimmer size, and corresponds to a distance somewhat shorter than the real-world distance from the cell body to the the end of its flagella.[65] As the forces are equal in magnitude, the swimmers are force-free, and their individual contributions to the fluid velocity field are therefore dipolar to leading order. The swimmers can be characterized by their dipole strength, $\kappa = Fl/\mu$ as presented in Eq. (2.9), the sign of which determines if it is a pusher ($\kappa > 0$) or a puller ($\kappa < 0$). In the case of a pusher, the forces are directed away from one another, while in the case of a puller they point towards each other. The model, specifically for the case of a pusher, is illustrated in Fig. 4.1.

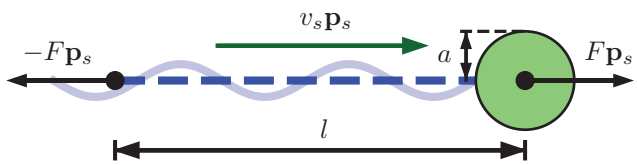

Figure 4.1 Schematic illustration of a pusher microswimmer modelled as an extended force dipole, along with its parameters.

The time evolution of a swimmer's position $\mathbf{r}_s$ and orientation $\mathbf{p}_s$ is given by the following equations of motion:[44,80]

$$\dot{\mathbf{r}}_s = v_s\mathbf{p}_s + \mathbf{U}(\mathbf{r}_s) \tag{4.1}$$

$$\dot{\mathbf{p}}_s = (\mathbb{I} - \mathbf{p}_s\mathbf{p}_s) \cdot (\beta\mathbf{E} + \mathbf{V}) \cdot \mathbf{p}_s \,, \tag{4.2}$$

where $\mathbf{U}(\mathbf{r}_s)$ is the fluid velocity evaluated at the position of the body of the swimmer, v_s is the swimming speed, and $\mathbb{I}$ is the unit tensor. Eq. (4.2) is Jeffery's equation, describing the reorientation of an ellipsoidal particle in a viscous fluid at low Reynolds number. $\beta = (\hat{q}^2 - 1)/(\hat{q}^2 + 1)$ is a shape parameter, with $\hat{q}$ denoting the ellipsoid aspect ratio, and $\mathbf{E} = (\nabla\mathbf{U} + \nabla\mathbf{U}^\dagger)/2$ and $\mathbf{V} = (\nabla\mathbf{U} - \nabla\mathbf{U}^\dagger)/2$ are, respectively, the rate-of-strain and vorticity tensors, evaluated at $\mathbf{r}_s$. Assuming an infinite aspect ratio, $\hat{q} = \infty \implies = 1$, and Eq. (4.2) simplifies to:

$$\dot{\mathbf{p}}_s = (\mathbb{I} - \mathbf{p}_s\mathbf{p}_s) \cdot (\nabla \mathbf{U}) \cdot \mathbf{p}_s \approx (\mathbb{I} - \mathbf{p}_s\mathbf{p}_s) \cdot \frac{\mathbf{U}(\mathbf{r}_s) - \mathbf{U}(\mathbf{r}_s - \mathbf{p}_s l)}{l}, \tag{4.3}$$

where the last equality is correct to linear order in the time step δt.

In addition to the reorientation caused by hydrodynamic interactions, the direction of the swimmer is randomized at Poisson distributed intervals of an average frequency λ, representing the tumble aspect of the run-and-tumble motion displayed by real bacteria. In the absence of other microswimmers and other forms of external forcing, these dynamics lead to a persistent random walk, with a persistence length of $l_p = v_s/\lambda$. This tumbling mechanism cannot however be included in a continuous-time differential equation, like that in Eq. (4.3), in a straightforward manner.

While the cell body radius a is specified above, it does not enter the equations of motion, nor does it directly relate to the swimming speed v_s or forces F exerted by the swimmer. As such, the model does not entail explicitly resolved bodies, and swimmers are effectively fore-aft symmetric, apart from their self-propulsion. The relation between F, l, and v_s can be utilized to calculate an effective hydrodynamic radius, and estimate the cell body radius a. To achieve this, we consider the force balance on the swimmer, relating the propulsive force $F\mathbf{p}_s$ acting on the flagella, with the Stokes' drag acting on the cell body.[44] In the absence of any external velocity field, this can be stated as

$$F\mathbf{p}_s = 6\pi\mu a \left(v_s\mathbf{p}_s - \mathbf{W}\right). \tag{4.4}$$

where $\mathbf{W}$ is the velocity field generated by the flagella, evaluated at the position of the cell body. In order for the drag force to be accurately described using Stokes' law, we assume that $(a/l)^2 \ll 1$, so that the velocity field has negligible gradients around the swimmer's body. $\mathbf{W}$ is approximated as the flow field due to a Stokeslet of equal magnitude and opposite sign to the propulsive force, located at the position of the flagella. From Eq. (2.6), we obtain the following expression:

$$\mathbf{W} = \frac{1}{8\pi\mu l}(\mathbb{I} + \mathbf{p}_s\mathbf{p}_s) \cdot (-F\mathbf{p}_s) = -\frac{1}{4\pi\mu l}F\mathbf{p}_s \tag{4.5}$$

This can be substituted into Eq. (4.4), yielding

$$v_s = \frac{F}{6\pi\mu a}\left(1 - \frac{3}{2}\frac{a}{l}\right) \equiv \frac{F}{6\pi\mu\tilde{a}} \tag{4.6}$$

The last equivalence introduces the effective hydrodynamic radius $\tilde{a}$, given by

$$\tilde{a} \equiv \frac{a}{1 - \frac{3}{2}\frac{a}{l}} \tag{4.7}$$

Given a set of model parameters, Eq. (4.6) can be used to obtain the effective cell body radius a. This in turn can be used for calculating approximate packing fractions, which allows for quantitative comparisons with experiments.

4.2.2 Other models

We now briefly consider two other computational swimmer models of wide use in active matter – the *squirmer* model, and the *slender rod* model.

In the former, microswimmers are modelled as spheres or ellipsoids with imposed velocity boundary conditions across their surfaces. It is arguably the most well-studied model of microswimmers, first developed by Blake in 1952,[87] and later refined to model the ciliated organism *Paramecium* (Fig. 1.2 right). In the case of a spherical swimmer displaying axisymmetric motion, expressions for the radial and tangential components of the slip velocity at the boundary are respectively given by[88]

$$v_r = \sum_{n=1}^{\infty} A_n P_n (\cos\theta) \tag{4.8}$$

and

$$v_\theta = \sum_{n=1}^{\infty} B_n V_n (\cos\theta), \tag{4.9}$$

where P_n is the n-th Legendre polynomial and V_n is defined by:

$$V_n(\cos\theta) = \frac{2}{n(n+1)} \sin\theta P'_n(\cos\theta), \tag{4.10}$$

where primes ($'$) denote derivatives with respect to the argument in the Legendre polynomials. θ is the polar angle relative to the swimming direction, as illustrated in Fig. 4.2. A_n and B_n are coefficients that characterize the details of the squirmer's propulsion. Especially the ratio B_2/B_1 is of relevance, as its sign determines if the

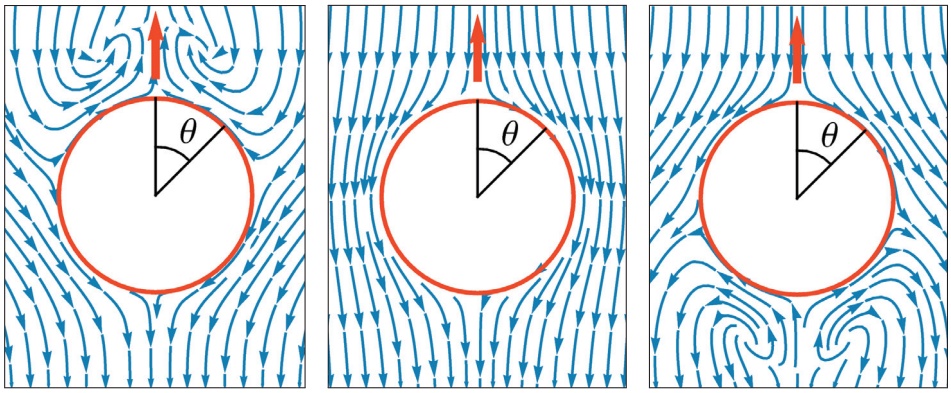

Figure 4.2 Illustrations of the fluid velocity fields around squirmers, as seen in the swimmers' frames of reference. They depict a pusher (left, reproduced from ref. 89), neutral swimmer (center, reproduced from ref. 90), and puller (right, reproduced from ref. 91).

flow field is puller-like (positive), or pusher-like (negative). In the case of $B_2/B_1 = 0$, the swimmer expresses neither characteristic, and is referred to as a *neutral* swimmer. The velocity fields generated by all three types of swimmer are displayed in Fig. 4.2. Some aspects of the collective behaviour of squirmers can be illustrated by considering a homogeneous suspensions of swimmers with an initial orientational alignment. In the case of pushers, orientations quickly decorrelate, while pullers aggregate together and display flocking with long-ranged polar order.[92]

In the slender rod model, swimmers are instead modelled as highly elongated ("slender") particles, which propel themselves by imposing a tangential shear stress on the fluid across a section of their surface, while the remainder of their body is subject to a no-slip boundary condition. The particle is effectively a pusher in the case of the shear stress being imposed near its rear, and a puller when it is imposed near the front.[36,93] In agreement with experiments and kinetic theory, a transition to active turbulence can be observed among slender rod pushers above a critical swimmer concentration, but not among pullers.[47,93,94]

4.3 Tracer models

In this thesis, we consider three types of tracer particles – point particles, spheres, and ellipsoids. For the first two, we consider only their translational motion, and they can thus be described by a single equation of motion. For point tracers, the EOM has a simple form:

$$\dot{\mathbf{r}}_t = \mathbf{U}(\mathbf{r}_t) + \sqrt{2D_0}\boldsymbol{\eta}, \tag{4.11}$$

where the first term represents simple advection by the fluid, and the second corresponds to Brownian motion. D_0 is the Brownian diffusion coefficient, and $\boldsymbol{\eta}$ is a unit-variance white noise, δ-correlated in space and time. Brownian motion is only considered for point particles, and the corresponding term will thus be omitted from the EOMs of the other tracer types.

In terms of forces acing on a point particle, there is a balance precisely when the tracer velocity $\mathbf{u}_t$ equals the fluid velocity $\mathbf{U}$, according to Stokes' law. If we instead consider spherical tracers, this force balance is however shifted. This is described by Faxén's law, which is a correction to Stokes' law for the frictional force $\mathbf{F}$ acting on a spherical object in a viscous fluid at low Reynolds number:[95-98]

$$\mathbf{F} = 6\pi\mu R_0 \left[\left(1 + \frac{R_0^2}{6}\Delta \right) \mathbf{U} - \mathbf{u}_t \right] \tag{4.12}$$

Here, R_0 is the radius of the spherical particle, and $\Delta \equiv \nabla^2$ is the Laplace operator. Force balance is realized when

$$\dot{\mathbf{r}}_t = \mathbf{u}_t = \left(1 + \frac{R_0^2}{6}\Delta \right) \mathbf{U}. \tag{4.13}$$

In our simulations, $\Delta\mathbf{U}$ is numerically evaluated with the finite difference method, using a seven-point stencil:

$$\Delta\mathbf{U}(\mathbf{r}) \approx \frac{1}{h^2}\Big(\mathbf{U}(\mathbf{r} - \mathbf{i}h) + \mathbf{U}(\mathbf{r} + \mathbf{i}h) + \mathbf{U}(\mathbf{r} - \mathbf{j}h) + \mathbf{U}(\mathbf{r} + \mathbf{j}h) + \mathbf{U}(\mathbf{r} - \mathbf{k}h) + \mathbf{U}(\mathbf{r} + \mathbf{k}h) - 6\mathbf{U}(\mathbf{r}) \Big) \tag{4.14}$$

where $\mathbf{i}$, $\mathbf{j}$ and $\mathbf{k}$ are the Cartesian basis vectors, and h is the discretization length over which the operator is numerically evaluated.

For ellipsoidal tracers, the translation is governed by Eq. (4.11). An extension of Faxén's law to ellipsoidal particles has been accomplished,[99,100] but is beyond the scope of this thesis. Reorientation of the particles is governed by Jeffery's equation, as in the case of swimmers. Assuming an infinite aspect ratio, one obtains

$$\dot{\mathbf{p}}_t = (\mathbb{I} - \mathbf{p}_t\mathbf{p}_t) \cdot (\nabla\mathbf{U}) \cdot \mathbf{p}_t \approx (\mathbb{I} - \mathbf{p}_t\mathbf{p}_t) \cdot \frac{\mathbf{U}(\mathbf{r}_t + \mathbf{p}_t h/2)) - \mathbf{U}(\mathbf{r}_t - \mathbf{p}_t h/2)}{h} \tag{4.15}$$

Equation (4.15) is similar to Eq. (4.3), with the only difference being that, in the case of a swimmer, the fluid velocity is evaluated at the cell body and the flagella, and rotation occurs around the former. In the case of an ellipsoidal tracer, the fluid velocity is evaluated at two points along the major axis, at equal distance from the particle center point around which the reorientation occurs. While the rotational EOM is that of an ellipsoid, the particles have no resolved bodies in this model, and thereby no defined size.

4.4 Lattice-Boltzmann methods

4.4.1 The Boltzmann equation and its discretization

The starting point of Lattice Boltzmann methods of fluid simulation, is the Boltzmann equation. [101] It describes the statistical behaviour of a system of particles, through the time evolution of their phase-space density function $f(\mathbf{r}, \mathbf{u}, t)$:

$$\frac{\partial f}{\partial t} + \mathbf{u} \cdot \nabla_{\mathbf{r}} f + \frac{\mathbf{F}}{m} \cdot \nabla_{\mathbf{u}} f = \Omega(f), \tag{4.16}$$

where $\mathbf{r}$ and $\mathbf{u}$ denotes particle position and velocity, and m is the particle mass. Ω is a so-called collision operator which represents the effect of collisions between particles, to be described below. f can be considered as a generalization of mass density ρ, as it simultaneously represents the density of mass in three-dimensional physical space, as well as three-dimensional velocity space. Originally the equation was formulated with application to actual molecules in mind. However, in the context of Lattice Boltzmann (LB) simulations, the particles considered are instead fictive, representing the fluid on a mesoscopic scale.

As indicated by its name, and briefly described in Section 4.1, the LB distribution function is simulated on a lattice. This corresponds to f being computed at discrete points in space, and at discrete time steps. The velocities of the particles involved are thus restricted to a finite set, represented by the vectors $\mathbf{c}_i$. This is illustrated in Fig. 4.3, showing one two-dimensional and one three-dimensional lattice system.

The set of allowed velocity vectors can be used to classify different LB methods by lattice type through the DdQq scheme, where d represents the dimensionality of the system and q is the number of available velocities. The set typically includes vectors pointing to the closest neighboring nodes, as well as a null vector representing stationary particles. As examples, let us consider the models displayed in Fig. 4.3. A particle in a D2Q9 system can move with a speed of 0, 1, or $\sqrt{2}$ lattice units δL per

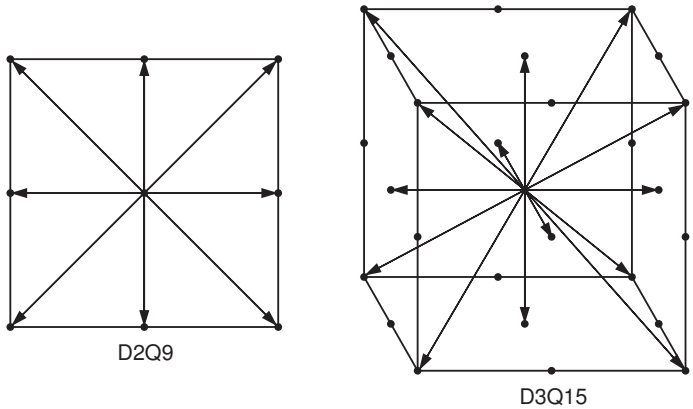

Figure 4.3 Illustration of a two-dimensional (left) and three-dimensional (right) LB lattice. Dots represent lattice nodes, on which f is computed, and arrows indicate the available velocity vectors $\mathbf{c}_i$ relative to the center point in the given DdQq scheme.

time step δt, corresponding to remaining at the same node, moving along the axes, or moving diagonally. In a D3Q15 lattice, which we employ in our simulations, the allowed speeds are 0, 1, or $\sqrt{3}$, respectively for being stationary, moving along the axes, or moving to the corners of the cube.

To facilitate the use of Eq. (4.16), we consider q different density functions $f_i(\mathbf{r}, t)$, $i \in \{0, q-1\}$, each representing particles moving with velocity $\mathbf{c}_i$. A discrete-velocity Boltzmann equation can then be considered for each given i:[102]

$$\frac{\partial f_i}{\partial t} + \mathbf{c}_i \cdot \nabla_{\mathbf{r}} f_i + \left[\frac{\mathbf{F}}{m} \cdot \nabla_{\mathbf{u}} f\right]_i = \Omega_i(f) \tag{4.17}$$

Given those f_i, macroscopic observables of the fluid can be obtained by calculating moments of the distribution functions. The fluid density ρ is expressed as

$$\rho = \sum_i f_i(\mathbf{r}, t), \tag{4.18}$$

while the fluid velocity is the average of the microscopic particle velocities:

$$\mathbf{U} = \frac{1}{\rho} \sum_i f_i(\mathbf{r}, t)\mathbf{c}_i \tag{4.19}$$

Rearranging Eq. (4.17) yields

$$\frac{\partial f_i}{\partial t} + \mathbf{c}_i \cdot \nabla_{\mathbf{r}} f_i = \Omega(f_i) - \left[\frac{\mathbf{F}}{m} \cdot \nabla_{\mathbf{u}} f\right]_i \equiv \Omega_i(f) + \Phi_i(\mathbf{r}, t). \tag{4.20}$$

On the right-hand side we now have a collision term Ω_i and a forcing term Φ_i, which we will consider in some more detail. Both of these have taken on different forms in different implementations of LBM. A common and relatively simple choice for Ω_i is the *Bhatnagar–Gross–Krook* (BGK) operator;[103,104]

$$\Omega_i(f) = -\frac{f_i(\mathbf{r}, t) - f_i^0(\mathbf{r}, t)}{T}. \tag{4.21}$$

Collisions described by this operator act to redistribute particles in phase space, so as to relax the system towards its equilibrium state f_i^0, given by a Maxwell-Boltzmann distribution. T is the relaxation time. A discrete representation of the equilibrium distributions can be obtained by considering their expansions in Hermite polynomials up to second order:[102]

$$f_i^0(\mathbf{r}, t) = w_i \rho \left(1 + \frac{\mathbf{U} \cdot \mathbf{c}_i}{c_s^2} + \frac{(\mathbf{U} \cdot \mathbf{c}_i)^2}{2c_s^4} - \frac{\mathbf{U} \cdot \mathbf{U}}{2c_s^2}\right), \tag{4.22}$$

where w_i are the weights of the velocity set $\{\mathbf{c}_i\}$, and c_s is the speed of sound in the medium. The weights w_i are generally not all equal, and their values in our specific implementation are presented in Section 4.4.3.

The forcing term Φ_i can be discretized in a similar manner, again employing a second order Hermite expansion:[105]

$$\Phi_i(\mathbf{r}, t) = \left(1 - \frac{\delta t}{2T}\right) w_i \left(\frac{\mathbf{c}_i - \mathbf{U}}{c_s^2} + \frac{(\mathbf{c}_i \cdot \mathbf{U})\mathbf{c}_i}{c_s^4}\right) \cdot \mathbf{f}(\mathbf{r}, t), \tag{4.23}$$

where $\mathbf{f}$ is the force density. We can now express the full *lattice Boltzmann equation* by discretizing Eq. (4.20):[102,103]

$$\bar{f}_i(\mathbf{r} + \mathbf{c}_i \delta t, t + \delta t) = \bar{f}_i(\mathbf{r}, t) - \frac{\delta t}{T + \delta t/2} \left(\bar{f}_i(\mathbf{r}, t) - f_i^0(\mathbf{r}, t) - \Phi_i(\mathbf{r}, t)\right), \tag{4.24}$$

where we have introduced a new set of density functions

$$\bar{f}_i(\mathbf{r}, t) = f_i(\mathbf{r}, t) - \frac{\delta t}{2}(\Omega_i(f) + \Phi_i(\mathbf{r}, t)). \tag{4.25}$$

The discrete time evolution of the system, as seen in Eq. (4.24), can be considered as the result of two separate processes. The first can be thought of as a collision step, in which the density functions relax towards their equilibrium states, considering particle collisions and external forces:

$$\bar{f}_i^*(\mathbf{r},t) = \bar{f}_i(\mathbf{r},t) - \frac{\delta t}{T+\delta t/2}\left(\bar{f}_i - f_i^0 - \Phi_i\right) \tag{4.26}$$

The second is a streaming step, where the density functions are allowed to propagate along the lattice, according to their velocities:

$$\bar{f}_i(\mathbf{r}+\mathbf{c}_i\delta t, t+\delta t) = \bar{f}_i^*(\mathbf{r},t) \tag{4.27}$$

In actual implementations of LBMs, these steps are alternated between. The algorithm is efficient, and was designed with parallelization in mind,[106] which is achievable due to the Lattice Boltzmann equation, as well as the collision and forcing terms, corresponding to entirely local dynamics.

4.4.2 Implementation of point forces

The discrete representation of the forcing term as seen in Eq. (4.23) considers a force density $\mathbf{f}$ acting on the lattice nodes, where f_i are computed. In many scenarios, the actual forces acting on the system will be defined off-lattice, and may even be modelled as force singularities. This is the case with the microswimmers described in this thesis – in particular section 4.2, and there is thus a need to interpolate such forces to the lattice nodes. We accomplish this through the use of a regularized version of the Dirac δ function, given by[107]

$$\delta^p(\mathbf{r}) = \frac{1}{(\delta L)^3} g\left(\frac{r_x}{\delta L}\right) g\left(\frac{r_y}{\delta L}\right) g\left(\frac{r_z}{\delta L}\right), \tag{4.28}$$

where δL is the lattice spacing, and $g(r)$ is defined by

$$g(r) = \begin{cases} \frac{3-2|r|+\sqrt{1+4|r|-4r^2}}{8}, & |r| \leq 1. \\ \frac{5-2|r|+\sqrt{-7+12|r|-4r^2}}{8}, & 1 \leq |r| < 2. \\ 0, & |r| \geq 2. \end{cases} \tag{4.29}$$

This procedure regularizes the forces over a support of two lattice units, effectively replacing the point forces with smooth but sharply peaked force density distributions.

The net force density at a given lattice node at $\mathbf{r}$ is obtained as a sum over all individual (regularized) point forces:

$$\mathbf{f}(\mathbf{r}) = \sum_{a=1}^{2N_s} \mathbf{F}'(\mathbf{r}_a)\delta^p(\mathbf{r} - \mathbf{r}_a), \tag{4.30}$$

where $\mathbf{F}'(\mathbf{r}_a)$ is the point force exerted at position $\mathbf{r}_a$. With N_s swimmers, and two forces per swimmer, there are thus $2N_s$ forces to interpolate. The same regularization was used for interpolating fluid velocities from the lattice nodes to the off-lattice swimmers, by summing over all N_* nodes at positions $\mathbf{r}_{N_*}$;

$$\mathbf{U}'(\mathbf{r}) = \sum_{N_*} \mathbf{U}(\mathbf{r}_{N_*})\delta^p(\mathbf{r} - \mathbf{r}_{N_*}), \tag{4.31}$$

4.4.3 Computational details

We employed a D3Q15 LBM, mainly using a cubic simulation box with a side length of 100 lattice units, and periodic boundary conditions. The weights of the velocity vectors $\mathbf{c}_i$ were set to $w_0 = 2/9$ for remaining in place, $w_1 - w_6$ to $1/9$ for moving along the axes, and $w_7 - w_{15}$ to $1/72$ for moving to the corners of the cube, as seen in Fig. 4.3. In terms of LB units, defined by the lattice spacing δL and time step length δt, the swimmer and fluid parameters were set to $F = 1.57 \times 10^{-3}$, $l = 1$, $\lambda = 2 \times 10^{-4}$, and if not specified otherwise, $v_s = 10^{-3}$. Lastly, μ was set to $1/6$, corresponding to the fluid relaxing to local equilibrium on each time step. The number of tracers was chosen as $N_t = 10^5$ for sufficient statistics. The swimmer Reynolds number of our system, assuming a density ρ of unity, is $\mathrm{Re} = \rho v_s l/\mu \approx 6 \times 10^{-3}$, confirming that we are in the low Reynolds number limit. We can further consider the non-dimensionalized dipole strength of our swimmers, $\kappa_n = F/(\mu l v_s) \approx 9.4$. This is similar to that of an actual *E. coli* bacterium, for which $F \approx 0.42$ pN, $l \approx 1.9$ µm, and $v_s \approx 22\ \mu m/s$, yielding $\kappa_n \approx 10.0$.[65]

5 Enhanced diffusion

5.1 Overview of tracer advection and diffusion by microswimmers

In suspensions of microswimmers, the diffusion of passive tracer particles is generally a complex function of both the swimming speed, dipole strength, tumbling rate, and number density of microswimmers. Here, we give an overview of different forms of interactions giving rise to tracer displacement – most of which are hydrodynamic in nature. It should be noted from the outset that, in the absence of swimmer-swimmer interactions, dipolar pushers and pullers are equivalent due to the symmetry of their individual flow fields. Experimentally, it has been observed that at low swimmer concentrations n, where swimmer-swimmer correlations are negligible, the translational diffusion coefficient D_T of tracers increases linearly with n.[38,41,43] The onset of collective behaviour among pushers coincides with a deviation from this linear dependence, building up to the turbulent state where D_T increases dramatically. This is due to the increased advection which follows from the enhanced fluid flow discussed previously. In puller suspensions on the other hand, correlations between swimmers suppresses the increase in diffusion, as swimmer-swimmer interactions decorrelate their orientations.

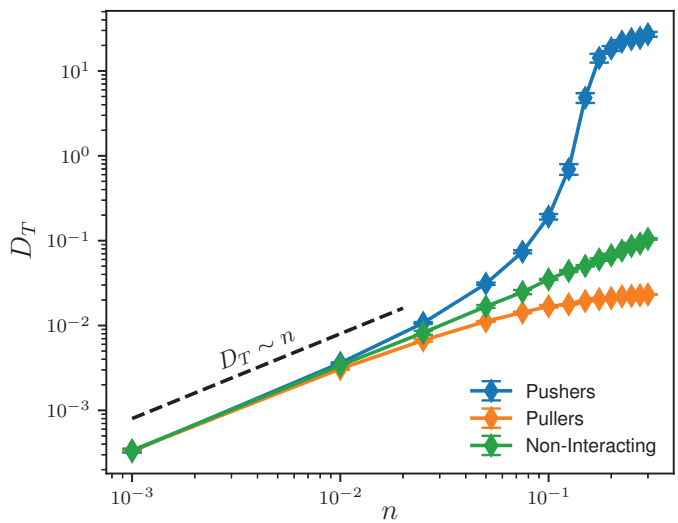

Figure 5.1 Effective translational diffusion coefficients of pushers, pullers, and non-interacting swimmers, as functions of swimmer number density n. Error bars denote one standard deviation as estimated from at least four separate runs with different initial conditions. Results are presented in terms of the swimmer length l and swimming timescale l/v_s.

In Fig. 5.1 we have reproduced the dependence of D_T on the swimmer number density n for pushers, pullers, and non-interacting swimmers, as previously discovered. [44-47] In our context, *non-interacting* swimmers refers to simulations in which hydrodynamic interactions between swimmers have been disabled, by setting the terms involving the fluid velocity $\mathbf{U}$ in their EOMs, Eqs. (4.1) and (4.3), to zero.

As this behaviour is readily observable in simulations such as ours, and can be rationalized in terms of the dipolar velocity fields of swimmers (see Section 3.2), enhanced tracer diffusion in microswimmer suspensions has largely been attributed to far-field hydrodynamic interactions. [44,46] While this behavior is relatively well understood, there are many aspects of tracer advection and enhanced diffusion in active suspensions that remain to be fully explained, some of which we address in the following sections.

The velocity field due to individual dipolar swimmers was described in Section 3.1, and the far field effects on swimmer-swimmer correlations was discussed in Section 3.2. Other interactions known to contribute to the displacement of tracer particles can be said to involve either near-field hydrodynamic effects, or be related to direct collisions between particles. [108] The nature of the latter is easy to comprehend, but its relative impact on the dynamics of an active matter system is in many cases poorly understood. Non-hydrodynamic effects such as electrostatic and van der Waals interactions between the tracers and microswimmers can also be considered, but will generally be specific to each experimental system, and are thus unlikely to account for widely observed diffusive phenomena.

Near-field hydrodynamic effects are due to the details of the short-ranged part of the swimmer flow field. For example, close to a microswimmer, the dipole approximation is no longer suitable for describing the velocity field. This is partly due to the detail of the swimmer's propulsion mechanism, but also due to the excluded volume effect of the cell body. Lubrication forces arise when two bodies are close to one another, but not in contact, and can lead to adhesive as well as repulsive interactions.

A clear example of a near-field effect known to impact tracer advection is so-called *entrainment*. [109,110] This can occur in cases where microswimmers are significantly larger than the passive particles, leading to the latter being effectively captured in a stagnation point of the swimmer's flow field. The tracer can then be carried over a large distance, before escaping and resuming regular diffusive motion. Individual tracer trajectories are therefore punctuated by very large displacements, and the displacement statistics are qualitatively different from Brownian motion and enhanced diffusion mediated by far-field hydrodynamic interactions. The effect depends on the propulsion mechanism of the swimmers, as well as the size of the considered tracers.

While near-field effects and particle collisions can have significant effects on tracer diffusion in microswimmer suspensions, they are not included in our simulations. This is a reasonable approximation when modelling small swimmers without stagnation points, like *E. coli*, immersed in bulk solutions where direct collisions are rare. This view is further supported by the good agreement between theory and simulations for enhanced diffusion measured in three-dimensional *E. coli* suspensions.[43]

5.2 Displacement of point tracers by dipolar swimmers

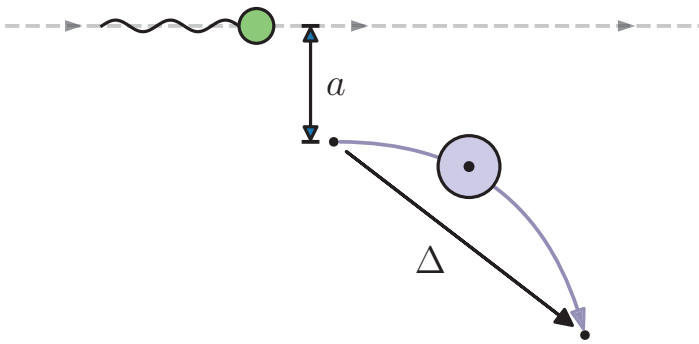

Figure 5.2 Illustration of a swimmer-tracer scattering event. a is the shortest distance between the swimmer's trajectory and the tracer's original position, and Δ is the tracer's net displacement during the scattering event. Reproduced from Paper III.

We now study the comparatively simple case of a single tracer advected by a dipolar swimmer, in the absence of Brownian motion. The swimmer travels in a straight line, with an initial swimmer-tracer separation a in the direction perpendicular to the swimming direction. This is illustrated in Fig. 5.2, and is informative for understanding enhanced diffusion, in particular before the onset of collective motion among the swimmers. For the case of the swimmer moving along an infinite straight path, the resulting tracer trajectory forms a closed loop, leading to a vanishing tracer net displacement Δ (Fig. 5.3a). When the swimmer's path is finite in length, the tracer's trajectory is effectively punctuated part-way through the loop, resulting in a significantly greater Δ (Fig. 5.3b). This resembles a scattering event due to a tumbling swimmer, and the effective advection caused between swimmer reorientations.

In the absence of swimmer-swimmer correlations, the total displacement of tracers, and therefore also their (active) diffusion coefficient D_A, can be seen as the result of a superposition of independent swimmer-tracer scattering events. While the displacement Δ due to any single scattering event depends on the tumbling rate λ, it has been shown that, in the limit of large self propulsion speeds v_s, D_A is in fact independent

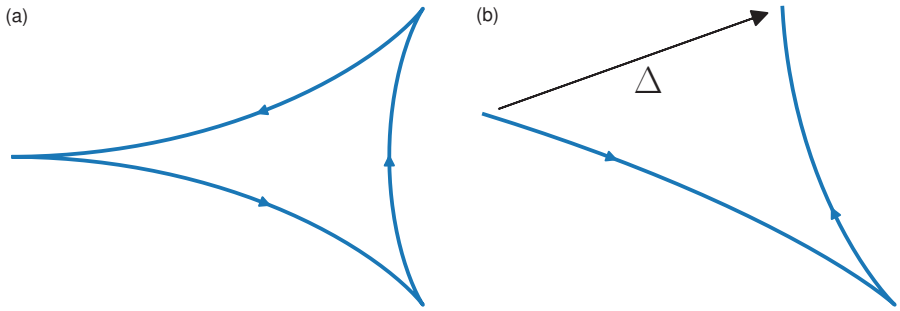

Figure 5.3 Examples of tracer trajectories due to scattering events, as illustrated in Fig. 5.2, obtained by integration of Eq. (2.8). (a) displays the trajectory due to a non-tumbling swimmer, following a straight, infinite path. (b) shows a trajectory due to an equivalent swimmer following a finite path, illustrating the effect a swimmer has on tracers between two tumbling events.

of λ.[111] A generalization of this result for finite v_s has later been derived, resulting in an approximate expression for the active diffusion coefficient D_A:[45]

$$D_A \approx \frac{7\kappa^2 n}{2048\lambda\varepsilon + 336\pi v_s}, \tag{5.1}$$

where ε is a characteristic size of the microswimmers, which we consider to be equal to the regularization length of the dipolar flow field. This expression captures the linear dependence of D_A with n seen below the onset of collective behaviour, and illustrates how both tumbling and swimming suppresses active diffusion, through λ and v_s respectively. We will revisit these effects in Section 5.4 and Paper II.

5.3 Computing diffusion coefficients

We have implemented two different methods of computing translational diffusion coefficients. The first relies on the mean-square displacement (MSD) of the tracers, and can be considered an extension of the expression for the displacement of a particle undergoing Brownian motion:

$$\mathrm{MSD}(\Delta t) \equiv \langle |\mathbf{r}_t(t_0 + \Delta t) - \mathbf{r}_t(t_0)|^2 \rangle = 2dD_T\Delta t, \tag{5.2}$$

where d is the dimensionality of the system. The MSD is obtained by averaging over all tracer particles, and all time origins t_0. In active suspensions, the MSD can instead be fitted using a persistent random walk model, characterized by a ballistic regime at

short times, and a diffusive regime beyond an effective crossover time τ_T. This results in the expression[112]

$$\mathrm{MSD}(\Delta t) = 2dD_T\left(\Delta t - \tau_T[1 - \exp\left(-\Delta t/\tau_T\right)]\right). \tag{5.3}$$

The other approach to computing translational diffusion coefficients relies on the Green-Kubo relation,

$$D_A = \frac{1}{3}\int_0^\infty \langle \dot{\mathbf{r}}_t(t)\cdot\dot{\mathbf{r}}_t(0)\rangle dt = \frac{1}{3}\int_0^\infty \langle \mathbf{U}(\mathbf{r}_t,t)\cdot\mathbf{U}(\mathbf{r}_t,0)\rangle \equiv \frac{1}{3}\int_0^\infty C_T(t)dt. \tag{5.4}$$

The last equality defines the velocity autocorrelation function $C_T(t)$ in the co-moving tracer frame. The relation assumes point-like tracers advected by the fluid, so that $\dot{\mathbf{r}}_t = \mathbf{U}(\mathbf{r}_t)$. It should be noted that while Eqs. (5.2) and (5.3) relates to the total effective diffusion coefficient, potentially including Brownian diffusion in addition to that caused by swimmer activity, Eq. (5.4) enables us to isolate the active diffusion coefficient D_A. Therefore, it is the method of choice in Section 5.4, where we consider the balance between D_A and the Brownian diffusion coefficient D_0. Eq. (5.4) can also be considered more robust than relying on MSD analyses, as no curve fitting is required. On the other hand, the Green-Kubo relation offers no way to directly obtain the crossover time τ_T, and cannot be directly implemented for computing diffusion coefficients along the different axes of anisotropic tracers. By applying both methods where possible, we have ensured that they yield equivalent results.

Where applicable, rotational diffusion coefficients of ellipsoidal tracers were calculated by fitting the orientational autocorrelation function $C_{\mathbf{p}}(\Delta t) \equiv \langle \mathbf{p}_t(t_0)\cdot\mathbf{p}_t(t_0+\Delta t)\rangle$ to the approximate expression[113]

$$C_{\mathbf{p}}(\Delta t) = \exp\left[-\frac{2D_R\Delta t^2}{\sqrt{4\tau_R^2+\Delta t^2}}\right]. \tag{5.5}$$

This expression can be said to interpolate between ballistic behavior at short times, $\left(C_{\mathbf{p}} = \exp\left[-(D_R/\tau_R)\Delta t^2\right]\right)$ and diffusive behavior beyond the effective crossover time τ_R, $\left(C_{\mathbf{p}} = \exp\left[-2D_R\Delta t\right]\right)$. It was first formulated by considering the random motion of a point on the surface of a sphere, in the case where the angular velocity is determined by an Ornstein-Uhlenbeck process.[113]

5.4 Balance of active and passive diffusion

In addition to being advected by the microswimmers in a suspension, tracer particles undergo Brownian motion due to thermal fluctuations. This is characterized by their thermal diffusion coefficient D_0. While the Brownian motion could initially be expected to increase the total diffusivity of particles, it has been hypothesized to suppress enhanced diffusion,[39] as random displacements disrupt swimmer-swimmer correlations and the spatiotemporal correlations of $\mathbf{U}(\mathbf{r}_t)$ along tracer trajectories. This is considered in more detail in Paper II, while we offer a brief overview here.

First, we consider the impact of some other parameters known to suppress D_A, namely the tumbling rate λ and propulsion speed v_s of the swimmers. This is displayed in Fig. 5.4, showing results of both LB simulations and predictions from kinetic theory (See paper II), in the absence of Brownian motion and swimmer-swimmer correlations. The active diffusion coefficient is shown to decrease monotonically with both parameters, with close agreement between theory and simulations. This behavior is due to the temporal decorrelation of the velocity field $\mathbf{U}(\mathbf{r}_t)$ when swimmers change direction (tumbling), or move significantly in relation to the tracer (self-propulsion).

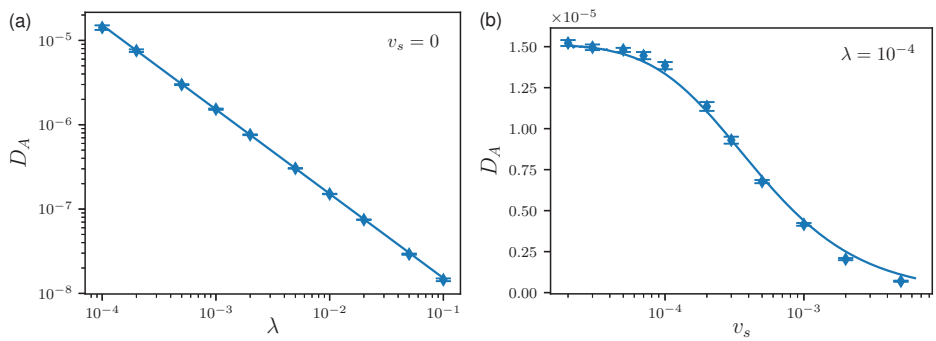

Figure 5.4 Active tracer diffusion in the absence of Brownian motion. (a) displays the λ^{-1} dependence of D_A in the case of ***shakers*** – swimmers with a vanishing propulsion speed. (b) displays the more complex dependence of D_A on v_s, at a fixed tumbling rate of $\lambda = 10^{-4}$. Symbols denote results from simulations, while solid lines show results from kinetic theory. Results are presented in LB units, and error bars denote one standard deviation as estimated from at least four separate runs with different initial conditions. Reproduced from Paper II.

To investigate the effect of Brownian motion, we define three dimensionless quantities for characterizing the system. The first is the *Péclet number*, which measures the relative importance of active and thermal forces, and which we define by

$$\mathrm{Pe} \equiv \frac{D_A(D_0 = 0)}{D_0}, \tag{5.6}$$

where $D_A(D_0 = 0)$ is the active diffusivity of tracers in an equivalent suspension,

but in the absence of Brownian motion. Secondly, we measure the change in active diffusion due to Brownian motion through the quantity

$$\xi \equiv \frac{D_A(D_0)}{D_A(D_0 = 0)}. \tag{5.7}$$

Lastly, the self-propulsion of swimmers is quantified by the non-dimensionalized swimmer persistence length L;

$$L \equiv \frac{v_s}{\varepsilon\lambda}. \tag{5.8}$$

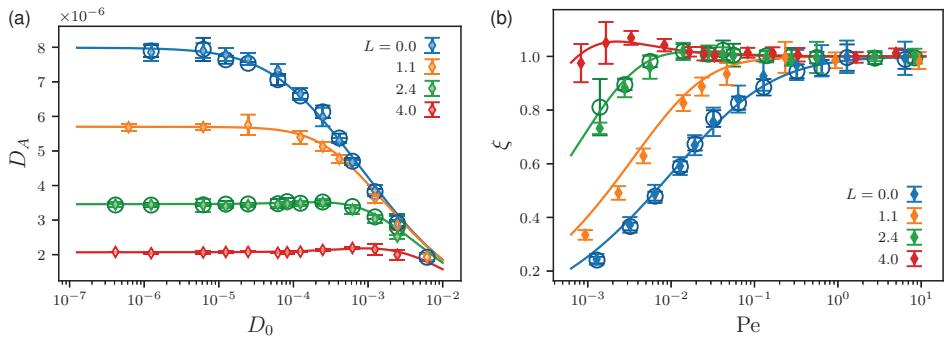

Figure 5.5 Decrease in active diffusion due to Brownian motion. (a) shows D_A as a function of D_0 for four different persistence lengths L, while (b) displays the same data expressed in the dimensionless quantities Pe and ξ. Error bars denote one standard deviation as estimated from four separate runs with different initial conditions. The circles for $L = 0$ and 2.4 correspond to the hydrodynamic diffusion in suspensions in which Brownian motion has been applied to the swimmers as opposed to the tracers, showing the two cases to be equivalent. Reproduced from Paper II.

In Fig. 5.5, we present the effect of varying the Brownian diffusion coefficient, for four different persistence lengths L. Active diffusion coefficients D_A were computed using the Green-Kubo relation, Eq. (5.4). From panel (a), it is immediately observable that D_A decreases with D_0, for large enough values of the latter. The change is most notable for $L = 0$, corresponding to "swimmers" that do not propel themselves, commonly referred to as *shakers*. The same data is presented in panel (b), but in terms of the Péclet number and ξ to better illustrate the effect of varying propulsion speed v_s. As ξ falls below unity, D_A is reduced compared to its non-Brownian value. In the case of shakers, this can be observed as soon as Pe < 1, while occurring at lower and lower values of Pe as L increases. For the fastest swimmers considered, $L = 4.0$, ξ remains close to unity in the whole observed range of Pe, indicating no suppression of D_A for values of Pe as low as 10^{-3}. This is notable, as a reduced persistence length of $L = 4$ still corresponds to relatively slow swimming in biological contexts. For comparison, estimates of L for *E. coli* bacteria lie in the range or 5 to 20,[45] suggesting that any effect of Brownian motion on D_A is likely negligible in bacterial suspensions,

in contrast with previous claims in the literature. Thus, while we have found D_0 to have a suppressive effect on active diffusion, this is unlikely to contribute to behavior seen among biological microswimmers, due to their relatively fast self-propulsion. This includes the non-monotonic dependence of D_A on tracer size,[39,114] discussed in Section 5.5.

5.5 Diffusion of spherical tracers

A fundamental aspect of Brownian motion is the inverse scaling of the passive diffusion coefficient D_0 with particle radius R_0, as described by the Stokes-Einstein relation.[115] In microswimmer suspensions, experimental observations have however shown this scaling not to hold, and the effective diffusivity D_T has been found to have a non-monotonic dependence on R_0, displaying a broad maximum for particles in the 1-10μm range.[39] This behavior has also been reproduced in simulations,[114] however the precise origin remains unclear due to the simultaneous effect of several types of interactions.

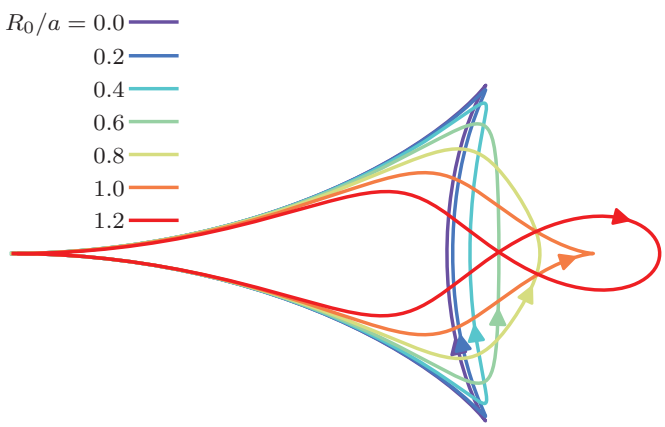

Figure 5.6 Trajectories of spherical tracers advected by a single swimmer moving along an infinite, straight path. Reproduced from Paper III.

The effect of Brownian motion has been discussed as a potential explanation of this non-monotonic behavior, but as argued in Section 5.4, such effects are likely negligible in suspensions of biological microswimmers, except at extremely low Péclet numbers. Other candidate mechanisms include tracer entrainment, which is expected to have a strong dependence on tracer size R_0. In Paper III, we explored whether modified

tracer advection due to Faxén's law, Eq. (4.12), could reproduce the dependence on R_0 seen in experiments, as the correction depends explicitly on tracer size. Here, we offer a brief overview.

We first considered the relatively simple case of a spherical tracer being advected by a single swimmer, similar to the scenario described in Section 5.2. When integrating over the tracer's trajectory, the Laplacian of the dipolar velocity field (Eq. (2.8)) at the position of the tracer could be analytically expressed as

$$\nabla^2 \mathbf{U}(\mathbf{r}_t; \mathbf{r}_s, \mathbf{p}_s) = \frac{3\kappa}{4\pi r'^5} \left[\left(1 - \frac{5}{r'^2} (\mathbf{r}' \cdot \mathbf{p}_s)^2 \right) \mathbf{r}' + 2(\mathbf{r}' \cdot \mathbf{p}_s) \mathbf{p}_s \right], \tag{5.9}$$

where $\mathbf{r}' = \mathbf{r}_t - \mathbf{r}_s$, and $r' = |\mathbf{r}'|$.

The results in the case of a swimmer moving along a straight, infinite path can be seen in Fig 5.6 for a range of tracer radii, rescaled by the shortest distance between the swimmer's trajectory and the tracer's original position. For a tracer radius of 0, the trajectory of a point tracer as seen in Fig. 5.2a is accurately reproduced. As the tracer size is increased, the two characteristic kinks in the $R_0 = 0$ loop are smoothed out. For $R_0/a = 1$, the appearance of a new kink can be seen, which then extends into an additional loop as $R_0/a > 1$. This regime is however unphysical, in the sense that the tracer radius is so large as to reach beyond the swimmer trajectory. The growing perturbations relative to $R_0 = 0$ show that Faxén's law has an impact on tracer trajectories, which could potentially affect diffusion coefficients.

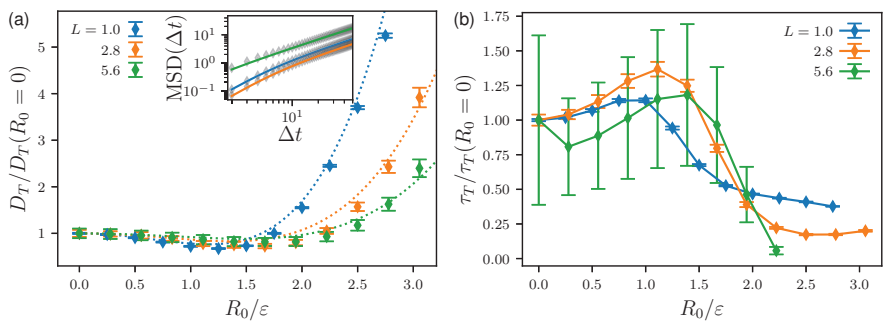

Figure 5.7 Tracer size dependence of D_T and τ_T. (a) $D_T(R_0)/D_T(0)$ for three different values of the reduced swimmer persistence length L, as indicated. Symbols indicate results from LB simulations, while dashed lines display predictions from kinetic theory. Inset shows mean-square displacement curves at $L = 2.8$ for $R_0/a = 0$ (blue), 1.4 (orange), and 2.8 (green) together with the respective fits to the persistent random walk model, Eq. (5.3). (b) Ballistic persistence time τ_T as obtained from LB simulations. For $R_0 > 2.3$ at $L = 5.6$ data is excluded since the quality of the fit is too poor to reliably determine τ_T. Reproduced from Paper III.

Next, we turn to the actual case of active diffusion, as induced by many individual scattering events. Starting in the dilute limit, we considered non-interacting swimmers, thus explicitly excluding swimmer-swimmer correlations. The results in Fig. 5.7 show the results from LB simulations and kinetic theory, expressing the change in D_T with R_0 due to the Faxén correction as $D_T(R_0)/D_T(R_0 = 0)$. In panel (a), a non-monotonic behavior is clearly observed for all three curves. However, while the agreement between simulations and kinetic theory is good, local minima are exhibited, rather than the maxima observed experimentally and numerically in previous works.[39,114] This is a clear indication that the experimentally observed behavior is not due to far-field hydrodynamic interactions. In panel (b), we display the persistence time τ_T of ballistic motion, as obtained by fitting to Eq. (5.3). All three curves show similar behavior, although uncertainties are significant for the largest studied L. τ_T exhibits an initial increase with R_0, before decreasing around $R_0/\varepsilon \approx 1$. Notably, the minima in panel (a) also occur around these radii, meaning when swimmers and tracers are of similar sizes. This suggest qualitative differences in behavior depending on which particle type is the largest.

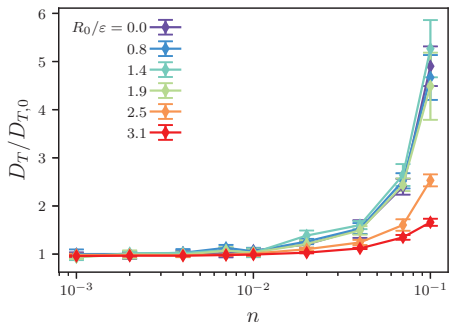

Figure 5.8 Effect of swimmer-swimmer correlations between pushers on tracer diffusion. The reduced diffusion coefficient $D_T/D_{T,0}$ is displayed as a function of swimmer concentration n for a range of reduced tracer radii R_0/ε.

Lastly, we considered suspensions of intermediate microswimmer density, where swimmer-swimmer correlations become significant. In Fig. 5.8, we display the active diffusion coefficient relative to its value in a suspension of non-interacting swimmers, $D_T/D_{T,0}$, as a function of swimmer density n and for a variety of reduced tracer radii R_0/ε. The figure specifically shows the case of pusher suspensions, and while the relative diffusion coefficient deviates from unity as n increases, it can be observed that increased tracer radius generally seems to reduce the effect of swimmer-swimmer correlations. A similar trend could also be observed for puller-type swimmers, although with deviations from unity being negative rather than positive.[116] However, it can also be discerned that the effect of swimmer-swimmer correlations are greatest around $R_0/\varepsilon = 1$, further indicating a qualitative change in behavior around this tracer size.

5.6 Diffusion of ellipsoidal tracers

It has been experimentally observed that tracer particles with shape asymmetry display anomalous anisotropic diffusion.[117,118] The effective drag on an elongated, ellipsoidal particle is expected to be smallest along its major axis, which through the Einstein relation suggests that the rate of Brownian diffusion be greatest in this direction.[119] This has indeed been observed to be the case of Brownian diffusion in bulk suspensions, where the ratio of diffusion coefficients parallel and perpendicular to the ellipsoid major axis $D_{||}/D_{\perp} \rightarrow 2$ for large tracer aspect ratios, due to their anisotropic friction.[120-122] In microswimmer suspensions confined to thin liquid films, $D_{||}/D_{\perp}$ has instead been found to fall below unity in the case of pushers (*E. coli*) at high densities.[117] In the case of puller-type swimmers (*C. Reinhardtii*), the ratio was instead observed to remain > 1,[118] in qualitative agreement with the behaviour in absence of swimmers. These results were partially explained in terms of the different symmetries of the flow fields of pushers and pullers in the qausi-2D geometry of their experimental system, and were ultimately attributed to the far-field dipolar fields generated by the swimmers.

In paper I, we investigated whether this anomalous anisotropic diffusion could be reproduced using LB simulations. In order to compute effective diffusion coefficients separately for directions parallel and perpendicular to the tracers' major axes, we employed a co-moving and co-rotating frame of reference for each particle. This approach is equivalent to that of Han et al.[121, 117,118], but extended from two to three dimensions. The total displacement of a tracer was computed by starting from its position and orientation in the laboratory frame at time step t_n, respectively $\mathbf{r}_t(t_n)$ and $\mathbf{p}_t(t_n)$. During the time interval between two time steps $\delta t = t_n - t_{n-1}$ the particle undergoes a translation $\delta\mathbf{r}_{t,n} = \mathbf{r}_t(t_n) - \mathbf{r}_t(t_{n-1})$. This is transformed into the tracer's body frame through the application of two subsequent rotations as seen in Fig. 5.9. This yields a body frame displacement

$$\delta\tilde{\mathbf{r}}_{t,n} = \mathbb{R}_y \cdot \mathbb{R}_z \cdot \delta\mathbf{r}_{t,n}, \tag{5.10}$$

where

$$\mathbb{R}_y = \begin{pmatrix} \cos\theta_{y,n} & 0 & \sin\theta_{y,n} \\ 0 & 1 & 0 \\ -\sin\theta_{y,n} & 0 & \cos\theta_{y,n} \end{pmatrix}, \tag{5.11}$$

$$\mathbb{R}_z = \begin{pmatrix} \cos\theta_{z,n} & \sin\theta_{z,n} & 0 \\ -\sin\theta_{z,n} & \cos\theta_{z,n} & 0 \\ 0 & 0 & 1 \end{pmatrix}. \tag{5.12}$$

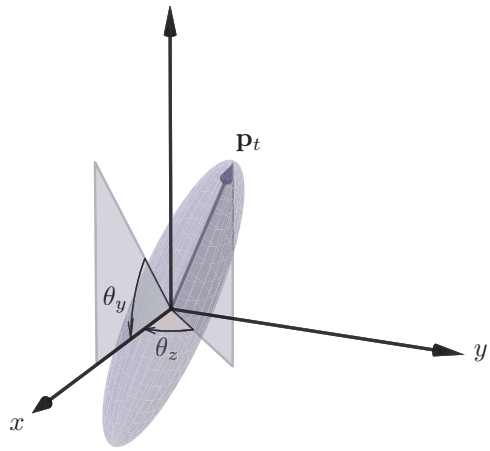

Figure 5.9 Schematic illustration of the rotation of an ellipsoidal tracer used for evaluating its displacement in the co-moving coordinate frame of reference.

The angles are averaged over time steps n and $n-1$, $\theta_{i,n} = [\theta_i(t_{n-1}) + \theta_i(t_n)]/2$, where θ_y is the angle between $\mathbf{p}_t$ and the lab xy plane and θ_z is the azimuthal angle between the x-axis and a projection of $\mathbf{p}_t$ onto the xy plane. By summing over all individual displacements $\delta\tilde{\mathbf{r}}_t$, n, the full body frame displacement over a macroscopic time interval t_n can be computed as

$$\tilde{\mathbf{r}}_t(t_n) = \sum_{k=1}^{n} \delta\tilde{\mathbf{r}}_{t,k}. \tag{5.13}$$

For trajectories of length Δt, the displacement in the body frame is given by $\Delta\tilde{\mathbf{r}}_t(\Delta t) = \tilde{\mathbf{r}}_t(t_0 + \Delta t) - \tilde{\mathbf{r}}_t(t_0)$. The first component of this quantity corresponds to the displacement along the particle's major axis, while the other two components represents the displacement in the plane perpendicular to this axis. For the computation of mean-square displacements, averaging was performed over all tracer particles, and over all time origins t_0 yielding trajectories of a given duration Δt. Translational diffusion coefficients were then obtained by fitting to Eq. (5.3), while rotational diffusion coefficients were calculated by fitting the orientational autocorrelation function to Eq. (5.5).

Before examining the anisotropic aspects of tracer diffusion, we considered the laboratory frame diffusion coefficients D_T and D_R as a function of swimmer density n. This is shown in Fig. 5.10, for the cases of pushers, pullers, and non-interacting swimmers. Both the translational and rotational diffusion coefficients are qualitatively analogous to the behaviour discussed in Fig. 5.1. At the lowest swimmer densities, all three

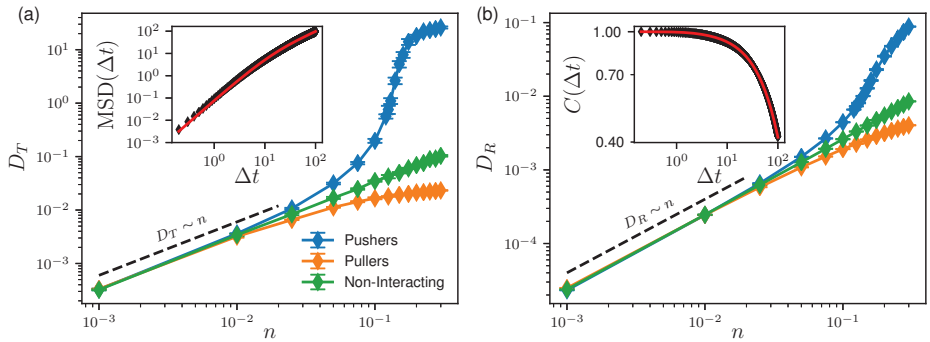

Figure 5.10 Translational and rotational diffusivity of ellipsoidal tracers, as measured in the laboratory frame. (a) and (b) display, respectively, the translational and rotational diffusion coefficients D_T and D_R as functions of swimmer density n. The inset in (a) shows an example of the translational MSD in a pusher suspension at $n = 0.1$, with a fit using Eq. (5.3), and the inset in (b) shows $C(\Delta t)$ in the same suspension, with a fit using Eq. (5.5). Error bars denote one standard deviation as estimated from at least four separate runs with different initial conditions. Results are presented in terms of the swimmer length l and swimming timescale l/v_s. Reproduced from Paper I.

swimmer types show a linear increase with n, before displaying significant deviations at intermediate concentrations ($0.01 < n < 0.2$), corresponding to the onset of swimmer-swimmer correlations. Pushers show a more steep increase in D_T and D_R with n, corresponding to the buildup towards bacterial turbulence, while pullers exhibit a slower increase. In the case of translational diffusion, this is in agreement with previous findings.[44,46,47] Furthermore, beyond the transition ($n > 0.2$) it can be observed that the translational diffusion coefficient of pushers deviates by approximately two orders of magnitude relative to the non-interacting value, while D_R deviates by one order of magnitude less. For pullers, the relative effect of correlations can also be seen to be smaller for rotation than translation. This can be explained by considering the decay law of the dipolar velocity fields generated by the swimmers. Tracer advection depends on the magnitude of the local velocity field, to which the contributions of individual swimmers scale as r^{-2}. The superposition of the fields generated by the whole suspension thus leads to truly long-ranged interactions. However, tracer rotation depend on the local velocity gradient, to which the contribution of a dipolar field decays as r^{-3}, and their superposition only yields a marginally long-ranged form of interaction. The correlation length of the velocity gradient field is therefore expected to be shorter, and thus D_R can be expected to be less affected than D_T by swimmer-swimmer correlations.

By decomposing the displacement as seen in the co-moving body frame, as described by Eqs. (5.10) to (5.13), the anisotropy of the translational diffusion can be quantified by considering the ratio of diffusion coefficients parallel end perpendicular to

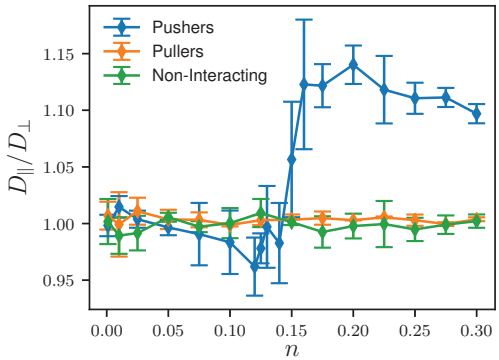

Figure 5.11 Anisotropic diffusion of ellipsoidal tracers, as measured in the co-moving body coordinate frame. The ratio of diffusion coefficients along the tracer major and minor axis is displayed as a function of n. Error bars denote one standard deviation as estimated from at least four separate runs with different initial conditions. Reproduced from Paper I.

the particle major axis, $D_{||}/D_{\perp}$, as displayed in Fig. 5.11. It can immediately be observed that suspensions of pullers and non-interacting swimmers display no discernible anisotropic diffusion, as the ratio remains close to unity across the whole range of swimmer densities. Pushers, however, display a sharp increase around $n = 0.15$, before stabilizing around $D_{||}/D_{\perp} \approx 1.1$. This occurrence coincides with the onset of active turbulence, as seen in Fig. 5.10. It is noteworthy that the steep increase in the ratio of diffusion coefficients appears significantly more well defined than the gradually growing deviation from linear behavior seen in Fig. 5.10, and therefore appears to be a potential signature of the transition to the turbulent state.

It is also obvious that the behavior of pushers seen in Fig. 5.11 is qualitatively different from experimental observations,[117] where $D_{||}/D_{\perp}$ decreases monotonically with n and falls well below unity after the onset of collective motion. This strongly suggest that, in unbounded three-dimensional systems, this type of anisotropy cannot be attributed to far-field hydrodynamic interactions as mediated by dipolar swimmers. Furthermore, previously presented arguments for the observed anisotropy in thin liquid films are based on tracer advection by a single swimmer, where both particles are confined to a two-dimensional plane while the swimmer dipole field is three-dimensional. Under this geometry, the equivalence between pushers and pullers at the single-swimmer level does not hold, and allows for different translation-rotation couplings for the two types of swimmers.[117] As this is prohibited in bulk 3D suspensions, such effects cannot yield different anisotropy for pushers and pullers in our system, in the absence of swimmer-swimmer correlations. However, as the anomalous translation-rotation coupling in liquid films is only experimentally observable at concentrations where swimmer-swimmer correlations are known to be significant,

single-swimmer effects are also indicated to be insufficient for describing the behaviour under such geometries. Instead, we suggest that the true origin of the anisotropic diffusion lies in other effects such as near-field hydrodynamic interactions or direct collisions between swimmers and tracers. Nevertheless, as 2D confinement is known to affect the hydrodynamic interactions between dipolar swimmers, simulations of such geometries could be fruitful, which is considered in Chapter 6.

6 Quasi-two dimensional systems

In this chapter, we briefly consider quasi-two dimensional microswimmer systems, and present previously unpublished results of LB simulations of anisotropic tracer diffusion in such geometries. As described is Section 5.6, for bacterial suspensions in thin liquid films, the ratio of diffusion coefficients parallel and perpendicular to ellipsoidal tracers' major axis $D_{||}/D_{\perp}$ falls below unity in the case of pushers at high densities, while remaining > 1 for pullers. This is in clear disagreement with the results of our simulations of three-dimensional microswimmer suspensions, also presented in Section 5.6. Motivated by these discrepancies, we investigated the impact of the system geometry on the diffusive behavior of ellipsoidal tracers. As opposed to the simulations presented in Chapter 5, we constructed a quasi-two dimensional system, by employing a simulation box with a quadratic base of $L_x = L_y = 100$ lattice units, and a thickness of $L_z = 9$ lattice units. Periodic boundary conditions were applied in the x-, and y-directions, while no-slip boundary conditions were applied in the z-direction. The positions and orientations of swimmers and tracers were confined to the mid-plane of the simulation box (at $z = L_z/2$), while the fluid was allowed to propagate also along the z-axis. The number of tracer particles included was reduced to $N_t = 20000$, due to the smaller system size.

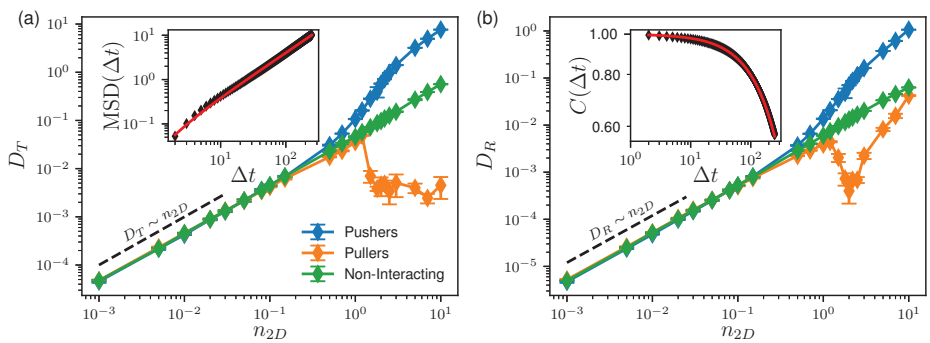

Figure 6.1 Translational and rotational diffusion of ellipsoidal tracers in a quasi-two dimensional system, as measured in the laboratory frame. (a) and (b) display, respectively, the translational and rotational diffusion coefficients D_T and D_R as functions of the two-dimensional swimmer density n_{2D}. The inset in (a) shows an example of the translational MSD in a pusher suspension at $n_{2D} = 0.2$, with a fit using Eq. (5.3), and the inset in (b) shows $C(\Delta t)$ in the same suspension, with a fit using Eq. (5.5). Error bars denote one standard deviation as estimated from at least four separate runs with different initial conditions. Results are presented in terms of the swimmer length l and swimming timescale l/v_s.

We begin by examining the laboratory frame diffusion coefficients D_T and D_R as functions of the two-dimensional swimmer density $n_{2D} = N_s/L_xL_y$, equivalent to our approach for the corresponding three-dimensional system shown in Fig. 5.10. As seen in Fig. 6.1, similar behavior can also be observed in the quasi-two dimensional system. At low swimmer concentrations D_T and D_R display linear scaling with n_{2D} for all three swimmer types. At intermediate densities ($0.1 < n_{2D} < 2$), both diffu-

sion coefficients exhibit a more steep increase with n_{2D} in the case of pushers, while increasing more slowly in the case of pullers. We identify this as the the onset of swimmer-swimmer correlations, which in the case of pushers is the buildup towards bacterial turbulence, analogous to what could be seen in three dimensions. Beyond this transition region, pullers however display behavior qualitatively different from that seen in Fig. 5.10. D_T decreases sharply by around one order of magnitude, and then remain largely constant. D_R initially shows a similar behavior, before increasing even more dramatically with increased n_{2D}, and approach the linear curve of non-interacting swimmers.

This behavior of pullers is a consequence of an instability associated with density variations, which arises due to the in-plane flow fields being effectively compressible, in spite of the incompressibility of the 3D bulk fluid.[123] As the fluid can move out-of-plane, dipolar swimmers act as sources (pushers) or sinks (pullers), with the latter showing a tendency to cluster together with their heads pointing towards a central point. The onset of such clustering is associated with a dramatic increase in the fluid mean-square velocity. This would be expected to increase the MSD of tracers, and thereby their translational diffusion coefficient, which is not reflected in Fig. 6.1. This might be due to the tracers becoming trapped in the sinks generated by clusters of pullers – a phenomenon that is in part unphysical due to excluded volume effects absent in our simulations.

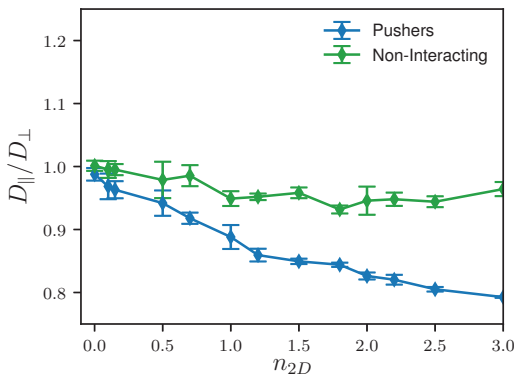

Figure 6.2 Anisotropic diffusion of ellipsoidal tracers in a quasi-two dimensional system, as measured in the co-moving body coordinate frame, analogous to Fig. 5.11. The ratio of diffusion coefficients along the tracer major and minor axis is displayed as a function of n_{2D}. Error bars denote one standard deviation as estimated from at least four separate runs with different initial conditions.

Next, we turn to the anisotropy of translational diffusion, by considering the ratio of diffusion coefficients parallel end perpendicular to the particle major axis, $D_{||}/D_{\perp}$. The results are presented in Fig. 6.2, analogous to the results for tree-dimensional suspensions displayed in Fig. 5.11. However, we exclude pullers due to the unphys-

ical aspects of their behavior following the instability just discussed. Non-interacting swimmers yield no anisotropic behavior in the whole observed range of n_{2D}, while pushers display a gradual decrease in $D_{||}/D_{\perp}$ with swimmer density. This is partly in agreement with experimental observations, which show that this ratio drops below unity for *E. coli* suspensions at intermediate densities.[117] However, due to the unavoidable inclusion of Brownian motion in any laboratory setting, anisotropic diffusion will be skewed towards the ellipsoid's major axis at low swimmer densities where advection is small, making direct comparison with Fig. 6.2 difficult. Nevertheless, the agreement in the trend of decreasing $D_{||}/D_{\perp}$ with n_{2D} in the case of pushers indicate that the geometry of the system might indeed partially explain their anisotropic diffusion in thin liquid films.

References

[1] Baxter, W. "A wedge of starlings", https://www.geograph.org.uk/photo/1069366, Licensed under CC BY 4.0. 03.03.2023.

[2] Hughes, R. https://commons.wikimedia.org/w/index.php?curid=61889652, Licensed under CC BY 4.0. 03.03.2023.

[3] Roper, M.; Dayel, M. J.; Pepper, R. E.; Koehl, M. A. R. Cooperatively Generated Stresslet Flows Supply Fresh Fluid to Multicellular Choanoflagellate Colonies. *Physical Review Letters* **2013**, *110*, 228104.

[4] Visser, A. W. Biomixing of the oceans? *Science* **2007**, *316*, 838–839.

[5] Lauga, E.; Powers, T. R. The hydrodynamics of swimming microorganisms. *Reports on Progress in Physics* **2009**, *72*, 096601.

[6] Ramaswamy, S. The mechanics and statistics of active matter. *Annual Review of Fluid Mechanics* **2010**, *1*, 323–345.

[7] Marchetti, M. C.; Joanny, J. F.; Ramaswamy, S.; Liverpool, T. B.; Prost, J.; Rao, M.; Simha, R. A. Hydrodynamics of soft active matter. *Reviews of Modern Physics* **2013**, *85*, 1143.

[8] Bialek, W.; Cavagna, A.; Giardina, I.; Mora, T.; Silvestri, E.; Viale, M.; Walczak, A. M. Statistical mechanics for natural flocks of birds. *Proceedings of the National Academy of Sciences of the United States of America* **2012**, *109*, 4786.

[9] Breder, C. Equations descriptive of fish schools and other animal aggregations. *Ecology* **1954**, *35*, 361–370.

[10] Ward, A. J. W.; Herbert-Read, J. E.; Jordan, L. A.; James, R.; Krause, J.; Ma, Q.; Rubenstein, D. I.; Sumpter, D. J. T.; Morrell, L. J. Initiators, Leaders, and Recruitment Mechanisms in the Collective Movements of Damselfish. *American Naturalist* **2013**, *181*, 748–760.

[11] Palacci, J.; Sacanna, S.; Steinberg, A. P.; Pine, D. J.; Chaikin, P. M. Living crystals of light-activated colloidal surfers. *Science* **2013**, *339*, 936–940.

[12] Saintillan, D.; Shelley, M. J. Active suspensions and their nonlinear models. *Comptes Rendus Physique* **2013**, *14*, 497.

[13] Creppy, A.; Praud, O.; Druart, X.; Kohnke, P. L.; Plouraboué, F. Turbulence of swarming sperm. *Physical Review E* **2015**, *92*, 032722.

[14] Wensink, H. H.; Dunkel, J.; Heidenreich, S.; Drescher, K.; Goldstein, R. E.; Löwen, H.; Yeomans, J. M. Meso-scale turbulence in living fluids. *Proceedings of the National Academy of Sciences of the United States of America* **2012**, *109*, 14308–14313.

[15] Dunkel, J.; Heidenreich, S.; Dreschner, K.; Wensink, H. H.; Bär, M.; Goldstein, R. E. Fluid dynamics of bacterial turbulence. *Physical Review Letters* **2013**, *110*, 228102.

[16] Cisneros, L. H.; Cortez, R.; Dombrowski, C.; Goldstein, R. E.; Kessler, J. O. Fluid dynamics of self-propelled microorganisms, from individuals to concentrated populations. *Experiments in Fluids* **2007**, *43*, 737.

[17] Vicsek, T.; Czirók, A.; Ben-Jacob, E.; Cohen, I.; Shochet, O. Novel Type of Phase Transition in a System of Self-Driven Particles. *Physical Review Letters* **1995**, *75*, 1226.

[18] Cates, M. E.; Tailleur, J. Motility-induced phase separation. *Annual Review of Condensed Matter Physics* **2015**, *6*, 219–244.

[19] Liu, G.; Patch, A.; Bahar, F.; Yllanes, D.; Welch, R. D.; Marchetti, M. C.; Thutupalli, S.; Shaevitz, J. W. Self-Driven Phase Transitions Drive Myxococcus xanthus Fruiting Body Formation. *Physical Review Letters* **2019**, *122*, 248102.

[20] Bunea, A.-I.; Taboryski, R. Recent Advances in Microswimmers for Biomedical Applications. *Micromachines* **2020**, *11*, 1048.

[21] Babu, S. B.; Stark, H. Modeling the locomotion of the African trypanosome using multi-particle collision dynamics. *New Journal Of Physics* **2012**, *14*, 085012.

[22] Oberholzer, M.; Lopez, M. A.; McLelland, B. T.; Hill, K. L. Social Motility in African Trypanosomes. *PLOS Pathogens* **2010**, *6*, 1–8.

[23] Maree, L.; van der Horst, G. Quantification and identification of sperm subpopulations using computer-aided sperm analysis and species-specific cut-off values for swimming speed. *Biotechnic & Histochemistry* **2013**, *88*, 181–193.

[24] Gomendio, M.; Roldan, E. R. S. Implications of diversity in sperm size and function for sperm competition and fertility. *International Journal Of Developmental Biology* **2008**, *52*, 439–447.

[25] Singh, A. V.; Ansari, M. H. D.; Dayan, C. B.; Giltinan, J.; Wang, S.; Yu, Y.; Kishore, V.; Laux, P.; Luch, A.; Sitti, M. Multifunctional magnetic hairbot for untethered osteogenesis, ultrasound contrast imaging and drug delivery. *Biomaterials* **2019**, *219*, 119394.

[26] Bhuyan, T.; Singh, A. K.; Dutta, D.; Unal, A.; Ghosh, S. S.; Bandyopadhyay, D. Magnetic Field Guided Chemotaxis of iMushbots for Targeted Anticancer Therapeutics. *ACS Biomaterials Science & Engineering* **2017**, *3*, 1627–1640.

[27] Srivastava, S. K.; Medina-Sanchez, M.; Koch, B.; Schmidt, O. G. Medibots: Dual-Action Biogenic Microdaggers for Single-Cell Surgery and Drug Release. *Advanced Materials* **2016**, *28*, 832–837.

[28] Erbe, E.; Pooley, C. Agricultural Research Center, USDA. https://www.ars.usda.gov/oc/images/photos/mar05/k11077-1/, https://commons.wikimedia.org/wiki/File:E_coli_at_10000x,_original.jpg, Licensed under CC BY 4.0. 04.03.2023.

[29] Dartmouth Electron Microscope Facility, Dartmouth College. http://remf.dartmouth.edu/imagesindex.html, https://commons.wikimedia.org/wiki/File:Chlamydomonas2-1.jpg, Licensed under CC BY 4.0. 04.03.2023.

[30] Mikhaltsov, A. https://commons.wikimedia.org/wiki/File:Paramecium_bursaria.jpg, Licensed under CC BY 4.0. 04.03.2023.

[31] Lele, P. P.; Roland, T.; Shrivastava, A.; Chen, Y.; Berg, H. C. The flagellar motor of Caulobacter crescentus generates more torque when a cell swims backwards. *Nature Physics* **2016**, *12*, 175+.

[32] Low, G.; Meister, M.; Berg, H. C. Rapid rotation of flagellar bundles in swimming bacteria. *Nature* **1987**, *325*, 637–640.

[33] Mitchell, D. R. *Chlamydomonas* flagella. *Journal of Phycology* **2000**, *36*, 261–273.

[34] Guasto, J. S.; Johnson, K. A.; Gollub, J. P. Oscillatory Flows Induced by Microorganisms Swimming in Two Dimensions. *Physical Review Letters* **2010**, *105*, 168102.

[35] Klindt, G. S.; Friedrich, B. M. Flagellar swimmers oscillate between pusher- and puller-type swimming. *Physical Review E* **2015**, *92*, 063019.

[36] Saintillan, D.; Shelley, M. J. Orientational order and instabilities in suspensions of self-locomoting rods. *Physical Review Letters* **2007**, *99*, 058102.

[37] Gibbons, I. R. Cilia and flagella of eukaryotes. *Journal of Cell Biology* **1981**, *91*, 107s–124s.

[38] Leptos, K. C.; Guasto, J. S.; Gollub, J. P.; Pesci, A. I.; Goldstein, R. E. Dynamics of enhanced tracer diffusion in suspensions of swimming eukaryotic microorganisms. *Physical Review E* **2008**, *77*, 026709.

[39] Patteson, A. E.; Gopinath, A.; Purohit, P. K.; Arratia, P. E. Particle diffusion in active fluids is non-monotonic in size. *Soft Matter* **2016**, *12*, 2365–2372.

[40] Kim, M. J.; Breuer, K. S. Enhanced diffusion due to motile bacteria. *Physics of Fluids* **2004**, *16*, 78.

[41] Miño, G.; Mallouk, T. E.; Darnige, T.; Hoyos, M.; Dauchet, J.; Dunstan, J.; Soto, R.; Wang, Y.; Rousselet, A.; Clement, E. Enhanced diffusion due to active swimmers at a solid surface. *Physical Review Letters* **2011**, *106*, 048102.

[42] Miño, G. L.; Dunstan, J.; Rousselet, A.; Clément, E.; Soto, R. Induced diffusion of tracers in a bacterial suspension. *Journal of Fluid Mechanics* **2013**, *729*, 423.

[43] Jepson, A.; Martinez, V. A.; Schwartz-Linek, J.; Morozov, A.; Poon, W. C. K. Enhanced diffusion of nonswimmers in a tree-dimensional bath of motile bacteria. *Physical Review E* **2013**, *88*, 041002.

[44] Stenhammar, J.; Nardini, C.; Nash, R. W.; Marenduzzo, D.; Morozov, A. Role of Correlations in the Collective Behavior of Microswimmer Suspensions. *Physical Review Letters* **2017**, *119*, 028005.

[45] Škultéty, V.; Nardini, C.; Stenhammar, J.; Marenduzzo, D.; Morozov, A. Swimming Suppresses Correlations in Dilute Suspensions of Pusher Microorganisms. *Physical Review X* **2020**, *10*, 031059.

[46] Qian, Y.; Kramer, P. R.; Underhill, P. T. Stochastic kinetic theory for collective behavior of hydrodynamically interacting active particles. *Physical Review Fluids* **2017**, *2*, 043104.

[47] Krishnamurthy, D.; Subramanian, G. Collective motion in a suspension of micro-swimmers that run-and-tumble and rotary diffuse. *Journal of Fluid Mechanics* **2015**, *781*, 422.

[48] Katija, K. Biogenic inputs to ocean mixing. *Journal Of Experimental Biology* **2012**, *215*, 1040–1049.

[49] Dewar, W. K.; Bingham, R. J.; Iverson, R. L.; Nowacek, D. P.; St. Laurent, L. C.; Wiebe, P. H. Does the marine biosphere mix the ocean? *Journal Of Marine Research* **2006**, *64*, 541–561.

[50] Mogre, S. S.; Brown, A., I; Koslover, E. F. Getting around the cell: physical transport in the intracellular world. *Physical Biology* **2020**, *17*, 061003.

[51] Lim, Y. F.; de Loubens, C.; Love, R. J.; Lentle, R. G.; Janssen, P. W. M. Flow and mixing by small intestine villi. *Food & Function* **2015**, *6*, 1787–1795.

[52] Argun, A.; Moradi, A.-R.; Pince, E.; Bagci, G. B.; Imparato, A.; Volpe, G. Non-Boltzmann stationary distributions and nonequilibrium relations in active baths. *Physical Review E* **2016**, *94*, 062150.

[53] Landau, L. D.; Lifshitz, E. M. *Fluid Mechanics*; Pergamin Press Ltd, 1959.

[54] Guazzelli, E.; Morris, J. F.; ; Sylvie, P. *A physical introduction to suspension dynamics*; Cambridge University Press: United Kingdom, 2012.

[55] Yeomans, J. M.; Pushkin, D. O. An introduction to the hydrodynamics of swimming microorganisms. *The European Physical Journal Special Topics* **2014**, *223*, 1771–1785.

[56] Happel, J.; Brenner, H. *Low Reynolds Number Hydrodynamics*; Martinus Nijhoff Publishers, 1983.

[57] Joseasorrentino, https://commons.wikimedia.org/wiki/File:Transicion_laminar_a_turbulento.png, Licensed under CC BY 4.0. 06.03.2023.

[58] Purcell, E. M. Life at low Reynolds number. *American Journal of Physics* **1977**, *45*, 3–11.

[59] Lauga, E. Life around the scallop theorem. *Soft Matter* **2011**, *7*, 3060–3065.

[60] Qiu, T.; Lee, T.-C.; Mark, A. G.; Morozov, K. I.; Münster, R.; Mierka, O.; Turek, S.; Leshansky, A. M.; Fischer, P. Swimming by reciprocal motion at low Reynolds number. *Nature Communications* **2014**, *5*, 5119.

[61] Brokaw, C. Microtubule sliding in swimming sperm flagella - direct and indirect measurements on sea-urchin and tunicate spermatozoa. *Journal of Cell Biology* **1991**, *114*, 1201–1215.

[62] Koyasu, S.; Shirakihara, Y. Caulobacter-crescentus flagellar filament has a right-handed helical form. *Journal of Molecular Biology* **1984**, *173*, 125–130.

[63] Oseen, C. *Hydrodynamik*; Akademische Verlagsgesellschaft, 1927.

[64] Hancock, G. J. The self-propulsion of microscopic organisms through liquids. *Proceedings of the royal society of London. Series A, Mathematical and physical sciences* **1953**, *217*, 96–121.

[65] Drescher, K.; Dunkel, J.; Cisneros, L. H.; Ganguly, S.; Goldstein, R. E. Fluid dynamics and noise in bacterial cell-cell and cell-surface scattering. *Proceedings of the National Academy of Sciences of the United States of America* **2011**, *108*, 10940–10945.

[66] Liao, Q.; Subramanian, G.; DeLisa, M. P.; Koch, D. L.; Wu, M. Pair velocity correlations among swimming Escherichia coli bacteria are determined by force-quadrupole hydrodynamic interactions. *Physics Of Fluids* **2007**, *19*, 061701.

[67] Guell, D. C.; Brenner, H.; Frankel, R. B.; Hartman, H. Hydrodynamic forces and band formation in swimming magnetotactic bacteria. *Journal of Theoretical Biology* **1988**, *135*, 525–542.

[68] Blake, J. R. A note on the image system for a stokeslet in a no-slip boundary. *Mathematical Proceedings of the Cambridge Philosophical Society* **1971**, *70*, 303–310.

[69] Ipina, E. P.; Otte, S.; Pontier-Bres, R.; Czerucka, D.; Peruani, F. Bacteria display optimal transport near surfaces. *Nature Physics* **2019**, *15*, 610+.

[70] Riedel, I. H.; Kruse, K.; Howard, J. A self-organized vortex array of hydrodynamically entrained sperm cells. *Science* **2005**, *308*, 300–303.

[71] Lauga, E.; DiLuzio, W. R.; Whitesides, G. M.; Stone, H. A. Swimming in circles: motion of bacteria near solid surfaces. *Biophysical Journal* **2006**, *90*, 400–412.

[72] Diluzio, W. R.; Turner, L.; Garstecki, M. M. P.; Weibel, D. B.; Berg, H. C. Escherichia coli swim on the right-hand side. *Nature* **2005**, *435*, 1271–1274.

[73] Park, Y.; Kim, Y.; Lim, S. Flagellated bacteria swim in circles near a rigid wall. *Physical Review E* **2019**, *100*, 063112.

[74] Pimponi, D.; Chinappi, M.; Gualtieri, P. Flagellated microswimmers: Hydrodynamics in thin liquid films. *European Physical Journal E* **2018**, *41*, 28.

[75] Saintillan, D.; Shelley, M. J. Instabilities and Pattern Formation in Active Particle Suspensions: Kinetic Theory and Continuum Simulations. *Physical Review Letters* **2008**, *100*, 178103.

[76] Hohenegger, C.; Shelley, M. J. Stability of active suspensions. *Physical Review E* **2010**, *81*, 046311.

[77] Doi, M.; Edwards, S. F. *The theory of polymer dynamics*; Clarendon Press, 1988.

[78] Balescu, R. *Equilibrium and Nonequilibrium Statistical Mechanics*; John Wiley and Sons: New York, 1975.

[79] Saintillan, D.; Shelley, M. J. Instabilities, pattern formation, and mixing in active suspensions. *Physics of Fluids* **2008**, *20*, 123304.

[80] Jeffery, G. B. The motion of ellipsoidal particles immersed in a viscous fluid. *Proceedings of the royal society of London. Series A, Mathematical and physical sciences* **1922**, *102*, 161.

[81] Subramanian, G.; Koch, D. L. Critical bacterial concentration for the onset of collective swimming. *Journal of Fluid Mechanics* **2009**, *632*, 359.

[82] Saintillan, D.; Shelley, M. J. Orientational order Instabilities in Suspensions of self-locomoting rods. *Physical Review Letters* **2007**, *99*, 058102.

[83] Doostmohammadi, A.; Ignés-Mullol, J.; Yeomans, J.; Sagués, F. Active nematics. *Nature Communications* **2018**, *9*, 3246–3246.

[84] Duclos, G.; Erlenkamper, C.; Joanny, J.-F.; Silberzan, P. Topological defects in confined populations of spindle-shaped cells. *Nature Physics* **2017**, *13*, 58–62.

[85] Sanchez, T.; Chen, D. T. N.; DeCamp, S. J.; Heymann, M.; Dogic, Z. Spontaneous motion in hierarchically assembled active matter. *Nature* **2012**, *491*, 431–434.

[86] Giomi, L.; Bowick, M. J.; Ma, X.; Marchetti, M. C. Defect Annihilation and Proliferation in Active Nematics. *Physical Review Letters* **2013**, *110*, 228101.

[87] Lighthill, M. J. On the squirming motion of nearly spherical deformable bodies through liquids at very small Reynolds numbers. *Communications on Pure and Applied Mathematics* **1952**, *5*, 109–118.

[88] Lauga, E. *The Fluid Dynamics of Cell Motility*; Cambridge University Press, 2020.

[89] Xammm, https://en.wikipedia.org/wiki/File:Pusher_squirmer,_swimmer_frame.png, Licensed under CC BY 4.0. 08.03.2023.

[90] Xammm, https://en.wikipedia.org/wiki/File:Neutral_squirmer,_swimmer_frame.png Licensed under CC BY 4.0. 08.03.2023.

[91] Xammm, https://en.wikipedia.org/wiki/File:Puller_squirmer,_swimmer_frame.png Licensed under CC BY 4.0. 08.03.2023.

[92] Alarcón, F.; Pagonabarraga, I. Spontaneous aggregation and global polar ordering in squirmer suspensions. *Journal of Molecular Liquids* **2013**, *185*, 56–61.

[93] Saintillan, D.; Shelley, M. J. Emergence of coherent structures and large-scale flows in motile suspensions. *Journal of the Royal Society Interface* **2012**, *9*, 571–585.

[94] Underhill, P. T.; Hernandez-Ortiz, J. P.; Graham, M. D. Diffusion and spatial correlations in suspensions of swimming particles. *Physical Review Letters* **2008**, *100*, 248101.

[95] Kim, S.; Karrila, S. J. *Microhydrodynamics*; Dover Publications, Inc.: New York, 2005.

[96] Faxén, H. Der Widerstand gegen die Bewegung einer starren Kugel in einer zähen Flüssigkeit, die zwischen zwei parallelen ebenen Wänden eingeschlossen ist. *Annalen der Physik* **1922**, *373*, 89–119.

[97] Chen, S. B.; Ye, X. Faxen's Laws of a Composite Sphere under Creeping Flow Conditions. *Journal of Colloid and Interface Science* **2000**, *221*, 50–57.

[98] Durlofsky, L.; Brady, J. F.; Bossis, G. Dynamic simulation of hydrodynamically interacting particles. *Journal of Fluid Mechanics* **1987**, *180*, 21–49.

[99] Hasimoto, H. An Extension of Faxen's Law to the Ellipsoid of Revolution. *Journal of the Physical Society of Japan* **1983**, *52*, 3294–3296.

[100] Phan-Thien, N.; Kim, S. *Microstructures in Elastic Media: Principles and Computational Methods*; Oxford University Press, 1994.

[101] Sukop, M. C.; Thorne, D. T. *Lattice Boltzmann modeling: An introduction for geoscientists and engineers*; Springer: Heidelberg, 2007.

[102] Nash, R. W.; Adhikari, R.; Cates, M. E. Singular forces and pointlike colloids in lattice Boltzmann hydrodynamics. *Physical Review E* **2008**, *77*, 026709.

[103] Krüger, T.; Kusumaatmaja, H.; Kuzmin, A.; Shardt, O.; Silva, G.; Viggen, E. M. *The lattice Boltzmann method - Principles and Practice*; Springer: Switzerland, 2017.

[104] Bhatnagar, P.; Gross, E.; Krook, M. A model for collision processes in gases .I. Small amplitude processes in charged and neutral one-component systems. *Physical Review* **1954**, *94*, 511–525.

[105] Guo, Z.; Zheng, C.; Shi, B. Discrete lattice effects on the forcing term in the lattice Boltzmann method. *Physical Review E* **2002**, *65*, 046308.

[106] Succi, S. *The Lattice Boltzmann Equation for Fluid Dynamics and Beyond*; Clarendon Press: Oxford, 2001.

[107] Peskin, C. S. The immersed boundary method. *Acta Numerica* **2002**, *11*, 479–517.

[108] Lagarde, A.; Dages, N.; Nemoto, T.; Demery, V.; Bartolo, D.; Gibaud, T. Colloidal transport in bacteria suspensions: from bacteria collision to anomalous and enhanced diffusion. *Soft Matter* **2020**, *16*, 7503–7512.

[109] Jeanneret, R.; Pushkin, D. O.; Kantsler, V.; Polin, M. Entrainment dominates the interaction of microalgae with micron-sized objects. *Nature Communications* **2016**, *7*, 12518.

[110] Shum, H.; Yeomans, J. M. Entrainment and scattering in microswimmer-colloid interactions. *Physical Review Fluids* **2017**, *2*, 113101.

[111] Pushkin, D. O.; Yeomans, J. M. Fluid Mixing by Curved Trajectories of Microswimmers. *Physical Review Letters* **2013**, *111*, 188101.

[112] Maggi, C.; Paoluzzi, M.; Pellicciotta, N.; Lepore, A.; Angelani, L.; Di Leonardo, R. Generalized Energy Equipartition in Harmonic Oscillators Driven by Active Baths. *Physical Review Letters* **2014**, *113*, 238303.

[113] Wilkinson, M.; Pumir, A. Spherical Ornstein-Uhlenbeck Processes. *Journal Of Statistical Physics* **2011**, *145*, 113–142.

[114] Dyer, O. T.; Ball, R. C. Influence of thermal fluctuations on active diffusion at large Peclet numbers. *Physics Of Fluids* **2021**, *33*, 051904.

[115] Einstein, A. *Investigations on the Theory of the Brownian Movement*; Dover Publications: New York, 1956.

[116] Nordanger, H.; Nüsslein, A.; Morozov, A.; Stenhammar, J. Size dependent hydrodynamic diffusion of spherical tracers in microswimmer suspensions. *Unpublished Manuscript* **2023**,

[117] Peng, Y.; Lai, L.; Tai, Y.-S.; Zhang, K.; Xu, X.; Cheng, X. Diffusion of Ellipsoids in Bacterial Suspensions. *Physical Review Letters* **2016**, *116*, 068303.

[118] Yang, O.; Peng, Y.; Liu, Z.; Tang, C.; Xu, X.; Cheng, X. Dynamics of ellipsoidal tracers in swimming algal suspensions. *Physical Review E* **2016**, *94*, 042601.

[119] Einstein, A. Über die von der molekularkinetischen Theorie der Wärme geforderte Bewegung von in ruhenden Flüssigkeiten suspendierten Teilchen. *Annalen der Physik* **1905**, *322*, 549–560.

[120] Dhont, J. *An Introduction to Dynamics of Colloids*; ISSN; Elsevier Science: New York, 1996.

[121] Han, Y.; Alsayed, A. M.; Nobili, M.; Zhang, J.; Lubensky, T. C.; Yodh, A. G. Brownian motion of an ellipsoid. *Science* **2006**, *314*, 626–630.

[122] Zheng, Z.; Han, Y. Self-diffusion in two-dimensional hard ellipsoid suspensions. *Journal Of Chemical Physics* **2010**, *133*, 124509.

[123] Škultéty, V.; Bárdfalvy, D.; Stenhammar, J.; Nardini, C.; Morozov, A. Hydrodynamic instabilities in a 2-D sheet of microswimmers embedded in a 3-D fluid. 2023; `https://arxiv.org/abs/2302.13966`.